The Raman Spectroscopy of Ionic Liquids

A Thesis presented in partial fulfilment of the requirements for the degree of

Master of Science in Chemical Physics

at

Massey University
New Zealand

Adam James Swanson
2007

Abstract

Raman and infrared spectra were recorded for the ionic liquids $[CH_3N(C_4H_8)Bu]^+[(F_3CSO_2)_2N]^-$, $[Et_3NH]^+[(octyl)PO_2H]^-$, $[Bu_4N]^+[(hexyl)PO_2H]^-$, and $[Bu_4P]^+[(octyl)_2PO_2]^-$ and was compared to spectra calculated by Gaussian 03 using the density functional theory method B3LYP. The experimental and calculated spectra were found to be very similar, indicating that no underlying anomalous effects were perturbing the vibrational modes. The peaks of the experimental and calculated Raman and infrared spectra were found to be broad and intertwined, because of the close proximity of numerous vibrational bands.

The differential and absolute scattering cross sections of selected bands of the ionic liquids were determined using a method of comparing the area of the ionic liquid's peak to standards of known cross section (cyclohexane, carbon tetrachloride, benzene, dichloromethane, and acetonitrile). Differential and absolute cross sections were determined experimentally at wavelengths 416 nm, 487 nm, 514 nm, 532 nm and 633 nm. A-term plots were constructed with these results to obtain the coupling constant and the effective excited state energy. These parameters allowed the calculation of the differential and absolute scattering cross sections at any wavelength.

This project is the first in a series of investigations to determine the electron transfer rate of ionic liquids and determine their suitability as materials in new devices.

Acknowledgements

I would like to thank my supervisor Dr Mark Waterland for his endless enthusiasm and encouragement throughout the highs and lows of this thesis. I would also like to thank the Massey University workshop team for their innovative, high quality and timely work on experimental apparatus. Finally, I would like to thank my family and Amanda for their support and encouragement. This work was able to be presented at the 2nd Australian Symposium on Ionic Liquids in Melbourne (11th-12th May 2006) and the NZIC Conference 2006 (2nd-6th December 2006) by funding from Massey University IFSGRF scholarships.

Contents

Abstract ii

Acknowledgments iii

Chapter 1

Introduction

1.0 Introduction 1

1.1 Classical formulation of Raman scattering 1

1.2 Quantum formulation of normal Raman scattering 3

1.3 Depolarization ratio 5

1.4 Theory of cross section measurements 7

1.5 Raman coefficients 8

1.6 A-Term fitting to cross sections 10

1.7 Wavelength dependent intensity corrections 11

1.8 Ionic liquids 12

1.9 Direction of work 14

Chapter 2

Experimental

2.0 Experimental introduction 15

2.1 Raman equipment setup 15

2.2 416 nm Raman experimental setup 15

2.3 487 nm and 514 nm Raman experimental setup 20

2.4 532 nm Raman experimental setup 23

2.5 633 nm Raman experimental setup 25

2.6 Depolarization ratio experiment 27

2.7 Frequency calibration 27

2.8 The spectrograph window 28

2.9 Beam dumping 29
2.10 Depolariser 29
2.11 Laser light filters 30
2.12 Collection procedure 31
2.13 416 nm collection 31
2.14 487 nm and 514 nm collection 32
2.15 532 nm collection 33
2.16 633 nm collection 34
2.17 Background collection 35
2.18 White light collection 35
2.19 Polarisation collection 35
2.20 Laser wavelength determination 36
2.21 Infrared experimental collection 36

Chapter 3

Gaussian Calculations

3.0 Gaussian calculations introduction 37
3.1 Raman calculations run 37
3.3 Raman calculation results 38
3.4 Infrared calculation results 51
3.5 Discussion of Gaussian calculations 63

Chapter 4

Raman and Infrared Band Assignments

4.0 Introduction to Raman and infrared band assignments 64
4.1 Raman band assignments 64

Chapter 5

A-Term Fitting to Raman Data

5.0 Introduction to A-term fitting to Raman data 68
5.1 Data processing for A-term graphs 68
5.2 A-term fitting to ionic liquid Raman data 71
5.3 Discussion of A-term fitting to Raman data 89

Chapter 6

Conclusion

6.0 Conclusion 92
6.1 Future work 93

References 94

List of Figures and Tables

Figure 1.1: Rayleigh, Stokes, and anti-Stokes scattering 3
Figure 2.1: 416 nm experimental configuration 16
Figure 2.2: Sample configuration for all wavelengths 17
Figure 2.3: Sample configuration used for all wavelengths 18
Figure 2.4: SRS generated 416 nm light illuminating an ionic liquid sample 19
Figure 2.5: SRS light separation after passing though one Pellin-Broca 20
Figure 2.6: Multi-line argon laser and the first Pellin-Broca setup 21
Figure 2.7: Pellin-Broca separating the light from the argon laser 21
Figure 2.8: 487 nm and 514 nm experimental configuration 22
Figure 2.9: 532 nm light from the YAG pulse laser illuminating a sample 23
Figure 2.10: 532 nm experimental configuration 24
Figure 2.11: HeNe laser used for generating 633 nm light 25
Figure 2.12: 633 nm experimental configuration 26
Figure 2.13: Polariser 27
Figure 2.14: Richard L. McCreery's standard 28
Figure 2.15: Setup of the 532 nm beam dump 29
Figure 2.16: Depolariser 30
Figure 2.17: Edge filter 31
Figure 3.1: Calculated Raman spectrum of $[Et_3NH]^+[(octyl)PO_2H]^-$ 39
Figure 3.2: Zoom plot of predicted Raman spectrum $[Et_3NH]^+[(octyl)PO_2H]^-$ 40
Figure 3.3: Experimental and predicted Raman spectrum $[Et_3NH]^+[(octyl)PO_2H]^-$ 42
Figure 3.4: Cation and anion of $[Et_3NH]^+[(octyl)PO_2H]^-$ 42
Figure 3.5: The calculated Raman spectrum $[Bu_4N]^+[hexylPO_2H]^-$ 44
Figure 3.6: Zoom plot of predicted Raman spectrum $[Bu_4N]^+[hexylPO_2H]^-$ 44
Figure 3.7: Experimental and predicted Raman spectrum $[Bu_4N]^+[hexylPO_2H]^-$ 46
Figure 3.8: Cation and anion of the ionic liquid $[Bu_4N]^+[hexylPO_2H]^-$ 46
Figure 3.9: Calculated Raman spectrum $[Bu_4P]^+[(octyl)_2PO_2]^-$ 48
Figure 3.10: Zoom plot of the predicted Raman spectrum $[Bu_4P]^+[(octyl)_2PO_2]^-$ 48
Figure 3.11: Experimental and predicted Raman spectrum $[Bu_4P]^+[(octyl)_2PO_2]^-$ 50
Figure 3.12: Cation and anion of $[Bu_4P]^+[(octyl)_2PO_2]^-$ 50
Figure 3.13: Calculated infrared spectrum $[Et_3NH]^+[(octyl)PO_2H]^-$ 52
Figure 3.14: Zoom plot of the predicted infrared spectrum $[Et_3NH]^+[(octyl)PO_2H]^-$ 52

Figure 3.15: Experimental and predicted infrared spectrum $[Et_3NH]^+[(octyl)PO_2H]^-$ 54
Figure 3.16: Calculated infrared spectrum $[Bu_4N]^+[(hexyl)PO_2H]^-$ 56
Figure 3.17: Zoom plot of the predicted infrared spectrum $[Bu_4N]^+[(hexyl)PO_2H]^-$ 56
Figure 3.18: Experimental and predicted infrared spectrum $[Bu_4N]^+[hexylPO_2H]^-$ 58
Figure 3.19: Calculated infrared spectrum $[Bu_4P]^+[(octyl)_2PO_2]^-$ 60
Figure 3.20: Zoom plot of the predicted infrared spectrum $[Bu_4P]^+[(octyl)_2PO_2]^-$ 60
Figure 3.21: Experimental and predicted infrared spectrum $[Bu_4P]^+[(octyl)_2PO_2]^-$ 62
Figure 3.22: The predicted spectrum of the anion PO_2H(hexyl) illustrating that numerous bands are involved in forming peaks 63
Figure 5.1: 742 cm^{-1} mode of $[CH_3N(C_4H_8)Bu]^+[(F_3CSO_2)_2N]^-$ fitted with gaussian curves 69
Figure 5.2: Differential scattering cross section vs. excitation energy for 742 cm^{-1} band of $[CH_3N(C_4H_8)Bu]^+[(F_3CSO_2)_2N]^-$ 74
Figure 5.3: Differential scattering cross section vs. excitation energy for 1241 cm^{-1} band of $[CH_3N(C_4H_8)Bu]^+[(F_3CSO_2)_2N]^-$ 76
Figure 5.4: Differential scattering cross section vs. excitation energy for 1300 cm^{-1} band of $[Et_3NH]^+[(octyl)PO_2H]^-$ 78
Figure 5.5: Differential scattering cross section vs. excitation energy for 1452 cm^{-1} band of $[Et_3NH]^+[(octyl)PO_2H]^-$ 80
Figure 5.6: Differential scattering cross section vs. excitation energy for 1447 cm^{-1} band of $[Bu_4N]^+[(hexyl)PO_2H]^-$ 82
Figure 5.7: Differential scattering cross section vs. excitation energy for 1298 cm^{-1} band of $[Bu_4P]^+[(octyl)_2PO_2]^-$ 84
Figure 5.7: Differential scattering cross section vs. excitation energy for 1447 cm^{-1} band of $[Bu_4P]^+[(octyl)_2PO_2]^-$ 86
Figure 5.8: Unphysical A-term fit for the 742 cm^{-1} band of $[CH_3N(C_4H_8)Bu]^+[(F_3CSO_2)_2N]^-$ 90
Figure 5.9: The replacement of multiple excited vibrational states with a single vibrational state for large ΔE 91
Table 3.1: Major Raman intensities $[Et_3NH]^+[(octyl)PO_2H]^-$ 38
Table 3.2: Comparison of $[Et_3NH]^+[(octyl)PO_2H]^-$ frequencies 41
Table3.3: Major Raman intensities $[Bu_4N]^+[hexylPO_2H]^-$ 43
Table 3.4: Comparison of $[Bu_4N]^+[hexylPO_2H]^-$ frequencies 45

Table 3.5: Major Raman intensities $[Bu_4P]^+[(octyl)_2PO_2]^-$ 47
Table 3.6: Comparison of $[Bu_4P]^+[(octyl)_2PO_2]^-$ frequencies 49
Table 3.7: Major infrared intensities $[Et_3NH]^+[(octyl)PO_2H]^-$ 51
Table 3.8: Comparison of $[Et_3NH]^+[(octyl)PO_2H]^-$ frequencies 53
Table 3.9: Major infrared $[Bu_4N]^+[(hexyl)PO_2H]^-$ 55
Table 3.10: Comparison of $[Bu_4N]^+[(hexyl)PO_2H]^-$ frequencies 57
Table3.11: Major infrared $[Bu_4P]^+[(octyl)_2PO_2]^-$ 59
Table 3.12: Comparison of $[Bu_4P]^+[(octyl)_2PO_2]^-$ frequencies 61
Table 4.1: Raman band assignments for $[Et_3NH]^+[(octyl)PO_2H]^-$ 64
Table 4.2: Raman band assignments for $[Bu_4N]^+[hexylPO_2H]^-$ 65
Table 4.3: Raman band assignments for $[Bu_4P]^+[(octyl)_2PO_2]^-$ 65
Table 4.4: Infrared band assignments for $[Et_3NH]^+[(octyl)PO_2H]^-$ 66
Table 4.5: Infrared band assignments for $[Bu_4N]^+[hexylPO_2H]^-$ 66
Table 4.6: Infrared band assignments for $[Bu_4P]^+[(octyl)_2PO_2]^-$ 67
Table 5.1: Differential scattering cross sections of known standards 69
Table 5.2: Refractive index and density of the ionic liquids 70
Table 5.3: Depolarization ratios of ionic liquid bands 72
Table 5.4: Differential scattering cross sections for 742 cm^{-1} band of $[CH_3N(C_4H_8)Bu]^+[(F_3CSO_2)_2N]^-$ 73
Table 5.5: Absolute scattering cross sections for 742 cm^{-1} band of $[CH_3N(C_4H_8)Bu]^+[(F_3CSO_2)_2N]^-$ 73
Table 5.6: Differential scattering cross sections for 1241 cm^{-1} band of $[CH_3N(C_4H_8)Bu]^+[(F_3CSO_2)_2N]^-$ 75
Table 5.7: Absolute scattering cross sections for 1241 cm^{-1} band of $[CH_3N(C_4H_8)Bu]^+[(F_3CSO_2)_2N]^-$ 75
Table 5.8: Differential scattering cross sections for 1300 cm^{-1} band of $[Et_3NH]^+[(octyl)PO_2H]^-$ 77
Table 5.9: Absolute scattering cross sections for 1300 cm^{-1} band of $[Et_3NH]^+[(octyl)PO_2H]^-$ 77
Table 5.10: Differential scattering cross sections for 1452 cm^{-1} band of $[Et_3NH]^+[(octyl)PO_2H]^-$ 79
Table 5.11: Absolute scattering cross sections for 1452 cm^{-1} band of $[Et_3NH]^+[(octyl)PO_2H]^-$ 79

Table 5.12: Differential scattering cross sections for 1447 cm^{-1} band of $[Bu_4N]^+[(hexyl)PO_2H]^-$ 81
Table 5.13: Absolute scattering cross sections for 1447 cm^{-1} band of $[Bu_4N]^+[(hexyl)PO_2H]^-$ 81
Table 5.14: Differential scattering cross sections for 1298 cm^{-1} band of $[Bu_4P]^+[(octyl)_2PO_2]^-$ 83
Table 5.15: Absolute scattering cross sections for 1298 cm^{-1} band of $[Bu_4P]^+[(octyl)_2PO_2]^-$ 83
Table 5.16: Differential scattering cross sections for 1447 cm^{-1} band of $[Bu_4P]^+[(octyl)_2PO_2]^-$ 85
Table 5.17: Absolute scattering cross sections for 1447 cm^{-1} band of $[Bu_4P]^+[(octyl)_2PO_2]^-$ 85
Table 5.18: Virtual excited state and differential coupling constant for standards 87
Table 5.19: Virtual excited state and differential coupling constant for ionic liquids 87
Table 5.20: Virtual excited state and absolute coupling constant for standards 88
Table 5.21: Virtual excited state and absolute coupling constant for ionic liquids 88

Chapter 1
Introduction

1.0 Introduction

This introduction is designed to give the reader an understanding of Raman spectroscopy and the concepts of scattering cross sections, depolarisation ratios and the A-term to aid with the interpretation of later chapters, particularly Chapter 5. The last part of this chapter outlines the interest in ionic liquids and the ionic liquids that will be studied in this thesis with the direction of this work outlined.

1.1 Classical Formulation of Raman Scattering

When light is scattered by matter the majority of the light is unscattered, known as Rayleigh scattering, and a very small amount of light is scattered at different frequencies, known as Raman scattering.

The electromagnetic fluctuations of the laser beam may be represented classically by:

$$E = E_0 \cos \omega_0 t = E_0 \cos 2\pi \nu_0 t$$

Where E_0 is the amplitude of the electric field and ν_0 is the frequency of the laser. When the electric field of the radiation interacts with an electron cloud of a chemical bond, then an electric dipole moment P is induced:

$$P = \alpha E = E_0 \cos 2\pi \nu_0 t$$

Where α is the polarizability of the molecule. If the molecule vibrates with a frequency ν_0 then the nuclear displacement q is given by:

$$q = q_0 \cos 2\pi \nu_m t$$

Where q_0 is the amplitude of the vibration. For small amplitude vibrations α is a linear function of q and we may perform a Taylor expansion:

$$\alpha = \alpha_0 + \left(\frac{\partial \alpha}{\partial q} \right)_0 q_0 + \ldots$$

Where α_0 is the polarizability at the equilibrium position and $(\partial\alpha/\partial q)_0$ is the rate of change of polarizability with respect to the change in q, evaluated at the equilibrium position.

Substituting the electric field, polarizability and nuclear displacement into the electric dipole moment equation we obtain:

$$P = \alpha E_0 \cos 2\pi\nu_0 t$$

$$= \alpha_0 E_0 \cos 2\pi\nu_0 t + \left(\frac{\partial\alpha}{\partial q}\right)_0 qE_0 \cos 2\pi\nu_0 t$$

$$= \alpha_0 E_0 \cos 2\pi\nu_0 t + \left(\frac{\partial\alpha}{\partial q}\right)_0 q_0 E_0 \cos 2\pi\nu_0 t \cos 2\pi\nu_m t$$

$$= \alpha_0 E_0 \cos 2\pi\nu_0 t + \frac{1}{2}\left(\frac{\partial\alpha}{\partial q}\right)_0 q_0 E_0 \left[\cos\left\{2\pi\left(\nu_0 + \nu_m\right)t\right\} + \cos\left\{2\pi\left(\nu_0 - \nu_m\right)t\right\}\right]$$

Using the trigonometric relation:

$$\cos x \cos y = \frac{1}{2}\left[\cos\left(x+y\right) + \cos\left(x-y\right)\right]$$

Where the first term of the electric dipole moment equation is Rayleigh scattering where light of the laser frequency ν_0 is emitted, the second term is anti-Stokes scattering where light of frequency $\nu_0+\nu_m$ is emitted and the third term is Stokes scattering where light of frequency $\nu_0-\nu_m$ is emitted.

Hence, in order to be Raman active the rate of change of polarizability with the vibration must be non-zero.

$$\left(\frac{\partial\alpha}{\partial q}\right)_0 > 0$$

Because $(\partial\alpha/\partial q)_0$ is small, Raman scattering is a weak effect [1].

In normal Raman spectroscopy the molecule is excited to some virtual state, ν_e, which is much lower in energy than the first electronic excited state. In Rayleigh scattering the molecule relaxes back to the lowest possible ground state, in Stokes scattering the molecule relaxes to the electronic ground state but remains in an excited vibrational state and in anti-Stokes scattering the molecule is excited from a vibrationally excited state then relaxes into the lowest possible ground state. The Stokes lines are much stronger than the anti-Stokes lines because of the Maxwell-Boltzmann distribution, which has the largest population of molecules being in the lowest possible ground state. Should the virtual excited state fall on an electronic excited state of the molecule we observe the phenomenon of resonance Raman scattering [2].

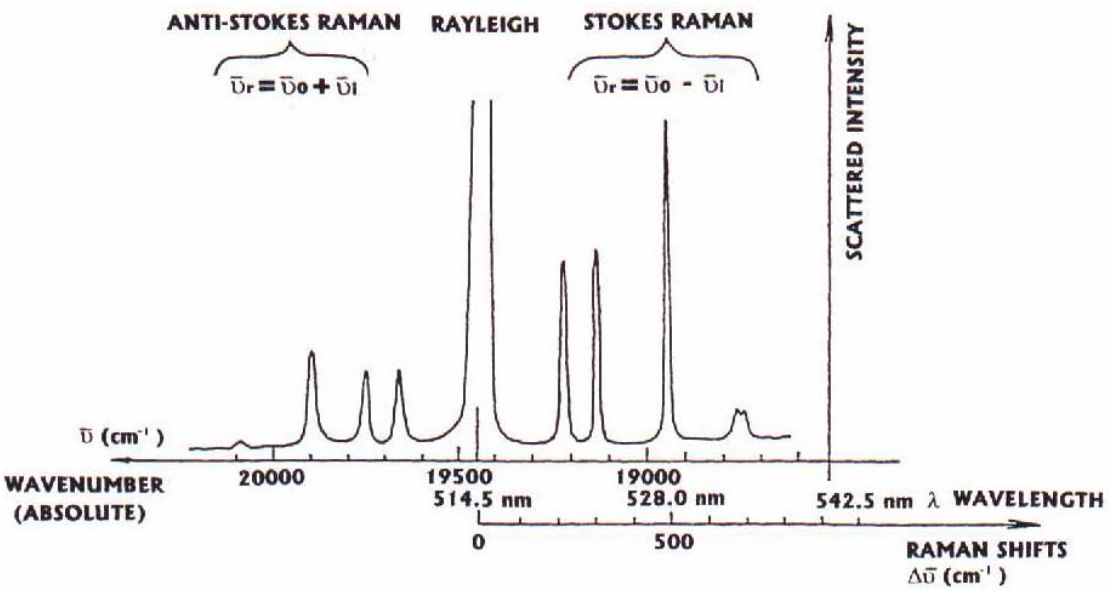

Figure 1.1: Rayleigh, Stokes, and anti-Stokes scattering generated from 514 nm Argon laser [3]

1.2 Quantum Formulation of Normal Raman Scattering

Using the adiabatic Born-Oppenheimer approximation, the vibrational states $|i\rangle$, $|f\rangle$ and $|r\rangle$ are formed by the multiplication of pure vibrational and pure electronic states. Making the assumption that the system is initially and finally in electronic state $|g\rangle$ we may write:

$$|i\rangle = |gm\rangle = |g\rangle|m\rangle$$

$$|f\rangle = |gn\rangle = |g\rangle|n\rangle$$

$$|r\rangle = |ev\rangle = |e\rangle|v\rangle$$

Where $|e\rangle$ is an excited electronic state and $|m\rangle, |n\rangle$ and $|v\rangle$ are vibrational states of the scattering molecule [4].

The corresponding transition polarizability may be written as [4]:

$$\left[\alpha_{\rho\sigma}\right]_{gn,gm} = \frac{1}{hc}\sum_{ev}\left(\frac{\langle n|\left[\mu_\rho\right]_{ge}|v\rangle\langle v|\left[\mu_\sigma\right]_{eg}|m\rangle}{\tilde{\nu}_{ev,gm} - \tilde{\nu}_0 + i\Gamma_{ev}} + \frac{\langle n|\left[\mu_\sigma\right]_{ge}|v\rangle\langle v|\left[\mu_\rho\right]_{eg}|m\rangle}{\tilde{\nu}_{ev,gn} + \tilde{\nu}_0 + i\Gamma_{ev}}\right)$$

Where $\tilde{\nu}_0$ is the frequency of the laser line, $\tilde{\nu}_{ev,gn}$ and $\tilde{\nu}_{ev,gm}$ are frequencies of the Raman transitions, $\left[\alpha_{\rho\sigma}\right]_{gngm}$ is the $\rho\sigma^{\text{th}}$ element of the transition polarizability tensor and $i\Gamma_{ev}$ is a damping term.

By invoking the closure relation $\sum_{v}|v\rangle\langle v|=1$ and using the fact that the denominators are large and insensitive to differences in the vibrational quantum numbers (*n*, *m* and *v*) we may neglect the differences between $\tilde{\nu}_{ev,gn}$ and $\tilde{\nu}_{ev,gm}$, and approximate to ν_e.

$$\left[\alpha_{\rho\sigma}\right]_{gn,gm}=\frac{1}{hc}\sum_{e}\left(\frac{\langle n|\left[\mu_\rho\right]_{ge}\left[\mu_\sigma\right]_{eg}|m\rangle}{\tilde{\nu}_e-\tilde{\nu}_0+i\Gamma_{ev}}+\frac{\langle n|\left[\mu_\sigma\right]_{ge}\left[\mu_\rho\right]_{eg}|m\rangle}{\tilde{\nu}_e+\tilde{\nu}_0+i\Gamma_{ev}}\right)$$

As $i\Gamma_{ev}\ll\tilde{\nu}_e-\tilde{\nu}_0,\tilde{\nu}_e+\tilde{\nu}_0$ we may neglect the damping term.

$$\left[\alpha_{\rho\sigma}\right]_{gn,gm}=\frac{1}{hc}\sum_{e}\left(\frac{\langle n|\left[\mu_\rho\right]_{ge}\left[\mu_\sigma\right]_{eg}|m\rangle}{\tilde{\nu}_e-\tilde{\nu}_0}+\frac{\langle n|\left[\mu_\sigma\right]_{ge}\left[\mu_\rho\right]_{eg}|m\rangle}{\tilde{\nu}_e+\tilde{\nu}_0}\right)$$

Using $\left(\tilde{\nu}_e-\tilde{\nu}_0\right)^{-1}+\left(\tilde{\nu}_e+\tilde{\nu}_0\right)^{-1}=2\tilde{\nu}_e\left(\tilde{\nu}_e^2-\tilde{\nu}_0^2\right)^{-1}$ the equation can be rewritten as:

$$\left[\alpha_{\rho\sigma}\right]_{gn,gm}=\frac{1}{hc}\sum_{e}\frac{2\tilde{\nu}_e\langle n|\left[\mu_\rho\right]_{ge}\left[\mu_\sigma\right]_{eg}|m\rangle}{\left(\tilde{\nu}_e^2-\tilde{\nu}_0^2\right)}$$

We may expand $\left[\mu_\rho\right]_{ge}$ as a Taylor series about the equilibrium position as the dependence of the dipole moment on the k^{th} normal nuclear coordinate of the system, Q_k, is small:

$$\left[\mu_\rho\right]_{ge}=\left[\mu_\rho\right]_{ge}^{0}+\sum_{k}\frac{\partial\left[\mu_\rho\right]_{ge}}{\partial Q_k}Q_k+\ldots$$

Higher order terms are small and may be neglected. The Born-Oppenheimer approximation allows the separation of the electronic and vibrational parts of the integral:

$$\langle n|\left[\mu_\rho\right]_{ge}|m\rangle=\left[\mu_\rho\right]_{ge}^{0}\langle n|m\rangle+\sum_{k}\frac{\partial\left[\mu_\rho\right]_{ge}}{\partial Q_k}\langle n|Q_k|m\rangle$$

Where $\langle n|m\rangle=\delta_{nm}$ with the Kronecker delta $\delta_{nm}=\begin{matrix}1\forall n=m\\0\forall n\neq m\end{matrix}$

Substituting back into the equation for polarizability:

$$\left[\alpha_{\rho\sigma}\right]_{gn,gm} = \frac{1}{hc}\sum_{e}\frac{2\tilde{\nu}_e}{\left(\tilde{\nu}_e^2-\tilde{\nu}_e^2\right)}\left[\mu_\rho\right]_{ge}^0\left[\mu_\sigma\right]_{eg}^0\langle n|m\rangle$$

$$+\frac{1}{hc}\sum_{e}\sum_{k}\frac{2\tilde{\nu}_e}{\left(\tilde{\nu}_e^2-\tilde{\nu}_0^2\right)}\left\{\frac{\partial\left[\mu_\rho\right]_{ge}}{\partial Q_k}\left[\mu_\sigma\right]_{eg}^0+\left[\mu_\rho\right]_{ge}^0\frac{\partial\left[\mu_\sigma\right]_{eg}}{\partial Q_k}\right\}\langle n|Q_k|m\rangle$$

$$+\frac{1}{hc}\sum_{e}\sum_{k,k'}\frac{2\tilde{\nu}_e}{\left(\tilde{\nu}_e^2-\tilde{\nu}_0^2\right)}\left\{\frac{\partial\left[\mu_\rho\right]_{ge}}{\partial Q_k}\frac{\partial\left[\mu_\sigma\right]_{eg}}{\partial Q_k}\right\}\langle n|Q_kQ_{k'}|m\rangle$$

Where n and m are vibrational quantum numbers of the ground electronic state. The first term corresponds to Rayleigh scattering as $\langle n|m\rangle=\delta_{nm}$. The second term corresponds to Stokes and anti-Stokes scattering as the integral is non-zero for $n=m\pm1$.

For $m=1$ Stokes scattering occurs and the integral equates to $\left[\frac{h(m+1)}{8\pi^2c\tilde{\nu}_k}\right]^{\frac{1}{2}}$.

For $m=-1$ anti-Stokes scattering occurs with the integral equating to $\left[\frac{hm}{8\pi^2c\tilde{\nu}_k}\right]^{\frac{1}{2}}$.

The third term is responsible for overtones $(k=k')$ and binary combination tones $(k\neq k')$. However, this effect is usually very weak in normal Raman scattering [4].

1.3 Depolarization Ratio

When electromagnetic radiation scatters off a sample, there is often a change in polarization. This scattered radiation can be completely or partially polarized. If the incident radiation is plane polarized or circularly polarized then changes of polarization state can be observed. These changes are important in Raman scattering as this may be correlated with the scattering species. A quantitative expression investigating such polarization changes is the depolarization ratio. We may define a scattering plane as the plane containing the direction of propagation of the incident radiation and the direction of observation (provided that no backscattering along the

direction of propagation occurs) [2]. For plane polarized light with the electric field vector parallel to the scattering plane a depolarization ratio may be defined as:

$$\rho_{\parallel}(\theta) = \frac{{}^{\parallel}I_{\perp}(\theta)}{{}^{\parallel}I_{\parallel}(\theta)}$$

Where θ is the angle between the direction of observation and the direction of propagation in the scattering plane. If the electric field vector is perpendicular to the scattering plane we may define the depolarization ratio as:

$$\rho_{\perp}(\theta) = \frac{{}^{\perp}I_{\parallel}(\theta)}{{}^{\perp}I_{\perp}(\theta)}$$

For natural radiation the depolarization ratio is defined as:

$$\rho_{n}(\theta) = \frac{{}^{n}I_{\parallel}(\theta)}{{}^{n}I_{\perp}(\theta)}$$

Ordinary depolarization ratios have values in the range $0 \leq \rho \leq 1$ for gases and liquids. For ρ being zero the light is completely polarized, for ρ being unity the light is natural and for values between zero and unity the light is partially polarized. Anomalous depolarization ratios can occur if an absorption band of the scattering system is close to the frequency of the incident radiation. In this case values of ρ much larger than unity are observed [2].

1.4 Theory of cross section measurements

A scattering cross section, σ, is a measure of the rate of the energy being removed from the incident beam due to scattering relative to the rate of energy of the incident beam passing through a unit area perpendicular to the direction of propagation. The scattering cross section has units of area, so any light passing through this area will be scattered. A differential cross section, $\partial\sigma/\partial\Omega$, may be defined as the power scattered into a given element of solid angle $\partial\Omega$. Both cross section and differential cross section are usually related to a single molecule [2].

We may express the differential cross section as:

$$\left(\frac{\partial\sigma}{\partial\Omega}\right)_1 \propto \frac{I_1 n_1^2}{\rho_1}$$

Where I_1 is the intensity of the Raman scattered light, n_1 is refractive index and ρ_1 is the density of the scattering liquid. We may take the ratio of an unknown liquid's cross section with a known standard's differential cross section:

$$\frac{\left(\frac{\partial\sigma_R}{\partial\Omega}\right)_1}{\left(\frac{\partial\sigma_R}{\partial\Omega}\right)_2} = \frac{I_1}{I_2}\left(\frac{n_1}{n_2}\right)^2 \frac{\rho_2}{\rho_1}$$

After rearranging we obtain:

$$\boxed{\left(\frac{\partial\sigma_R}{\partial\Omega}\right)_1 = \frac{I_1}{I_2}\left(\frac{n_1}{n_2}\right)^2 \frac{\rho_2}{\rho_1}\left(\frac{\partial\sigma_R}{\partial\Omega}\right)_2}$$

Hence by knowing the refractive index and density of the standard and sample, and the differential cross section of the standard, we may take a ratio of the standard and samples Raman scattering peaks to determine the sample's differential cross section.

Experimentally we measure differential cross sections, which can be converted to absolute cross sections by using the following relationship:

$$\frac{\partial\sigma_R}{\partial\Omega} = \frac{3}{8\pi}\left(\frac{1+\rho}{1+2\rho}\right)\sigma_R$$

In this case ρ refers to the depolarization ratio and is not to be confused with density given by earlier equations [5, 6]. This can be rearranged to give:

$$\boxed{\sigma_R = \frac{8\pi}{3}\left(\frac{1+2\rho}{1+\rho}\right)\frac{\partial\sigma_R}{\partial\Omega}}$$

1.5 Raman coefficients

Using the equation for the transition polarizability defined earlier for normal Raman scattering we can now consider the special case of resonance Raman scattering where the virtual excited state falls on an electronic state of the molecule [4].

$$\left[\alpha_{\rho\sigma}\right]_{gn,gm} = \frac{1}{hc}\sum_{ev}\left(\frac{\langle n|\left[\mu_\rho\right]_{ge}|v\rangle\langle v|\left[\mu_\sigma\right]_{eg}|m\rangle}{\tilde{\nu}_{ev,gm}-\tilde{\nu}_0+i\Gamma_{ev}}+\frac{\langle n|\left[\mu_\sigma\right]_{ge}|v\rangle\langle v|\left[\mu_\rho\right]_{eg}|m\rangle}{\tilde{\nu}_{ev,gn}+\tilde{\nu}_0+i\Gamma_{ev}}\right)$$

Assuming that the adiabatic Born-Oppenheimer approximation is valid, other assumptions are regarded to no longer hold:

1. The ν dependence of the denominator can no longer be ignored and the closure theorem can not be used.
2. The wavenumber difference $\left(\tilde{\nu}_{ev,gm}-\tilde{\nu}_0\right)$ of the denominator is of the order of the damping factor $i\Gamma_{ev}$ meaning the damping factor can not be ignored.
3. The first order term $\left[\mu_\rho\right]'_{ge}$ of the Taylor expansion for the pure electronic transition moment can not be ignored and needs to be defined explicitly.

Using the Hertzberg-Teller perturbation, which is valid for weak coupling, the derivative of the transition dipole moment arises from the variation of the Hamiltonian with respect to the normal coordinate; allowing state $|e\rangle$ to mix with other states $|s\rangle$ of appropriate symmetry [4]. Therefore we may write:

$$\left[\mu_\rho\right]_{ge} = \left[\mu_\rho\right]^0_{ge} + \sum_s\sum_k\left[\mu_\rho\right]^0_{gs}\frac{h^k_{es}}{\Delta\tilde{\nu}_{es}}Q_k + \ldots$$

$$h^k_{es} = \langle e|\frac{\partial\hat{H}}{\partial Q_k}|s\rangle_{Q_{k=0}}$$

Where $|s\rangle$ represents another excited state and $\frac{h^k_{es}}{\Delta\tilde{\nu}_{es}}$ is the strength of the vibronic coupling of states $|e\rangle$ and $|s\rangle$ via the normal coordinate. The transition polarizability

can be simplified by making use of resonance conditions: as $\tilde{\nu}_0$ approaches the excited state, $\tilde{\nu}_{ev,gm}$ will dominate the sum over states. Hence, it is sufficient to consider only one or two electronic manifolds. The resonance conditions also allow the non-resonant components to be ignored [4]. Applying these new considerations to the transition polarizability defined for normal Raman scattering we obtain an equation for the transition polarizability that has four contributions, the A, B, C and D terms:

$$\left[\alpha_{\rho\sigma}\right]_{gn,gm} = A + B + C + D$$

Where

$$A = \frac{1}{hc}\left[\mu_\rho\right]^0_{ge}\left[\mu_\sigma\right]^0_{eg}\sum_v \frac{\langle n_g|v_e\rangle\langle v_e|m_g\rangle}{\tilde{\nu}_{ev,gm} - \tilde{\nu}_0 + i\Gamma_{ev}}$$

$$B = \frac{1}{h^2c^2}\sum_{s\neq e}\left[\mu_\rho\right]^0_{gs}\left[\mu_\sigma\right]^0_{eg}\frac{h^k_{se}}{\Delta\tilde{\nu}_{se}}\sum_v \frac{\langle n_g|Q_k|v_e\rangle\langle v_e|m_g\rangle}{\tilde{\nu}_{ev,gm} - \tilde{\nu}_0 + i\Gamma_{ev}} + \frac{1}{h^2c^2}\sum_{s\neq e}\left[\mu_\rho\right]^0_{ge}\left[\mu_\sigma\right]^0_{sg}\frac{h^k_{es}}{\Delta\tilde{\nu}_{es}}\sum_v \frac{\langle n_g|v_e\rangle\langle v_e|Q_k|m_g\rangle}{\tilde{\nu}_{eg,gm} - \tilde{\nu}_0 + i\Gamma_{ev}}$$

$$C = \frac{1}{h^2c^2}\sum_{s\neq g}\left[\mu_\rho\right]^0_{se}\left[\mu_\sigma\right]^0_{eg}\frac{h^k_{gs}}{\Delta\tilde{\nu}_{gs}}\sum_v \frac{\langle n_g|Q_k|v_e\rangle\langle v_e|m_g\rangle}{\tilde{\nu}_{ev,gm} - \tilde{\nu}_0 + i\Gamma_{ev}} + \frac{1}{h^2c^2}\sum_{s\neq g}\left[\mu_\rho\right]^0_{ge}\left[\mu_\sigma\right]^0_{es}\frac{h^k_{sg}}{\Delta\tilde{\nu}_{sg}}\sum_v \frac{\langle n_g|v_e\rangle\langle v_e|Q_k|m_g\rangle}{\tilde{\nu}_{ev,gm} - \tilde{\nu}_0 + i\Gamma_{ev}}$$

$$D = \frac{1}{h^3c^3}\sum_{s,s'\neq e}\left[\mu_\rho\right]^0_{gs}\left[\mu_\sigma\right]^0_{s'g}\frac{h^k_{es}h^{k'}_{es'}}{\Delta\tilde{\nu}_{es}\Delta\tilde{\nu}_{es'}}\sum_v \frac{\langle n_g|Q_k|v_e\rangle\langle v_e|Q_{k'}|m_g\rangle}{\tilde{\nu}_{ev,gm} - \tilde{\nu}_0 + i\Gamma_{ev}}$$

To simplify our calculations we only consider the dominant A-term. In the next section the A-term is linked to the scattering cross section of a molecule.

1.6 A-Term fitting to cross sections

The expression for preresonance cross section is given by:

$$\left(\sigma_R\right)_{m,n} = \frac{2^7 \pi^5 \nu^4}{3^2 c^4}\left(\alpha_{m,n}\right)^2$$

Where υ is the scattered frequency of the radiation and $\alpha_{m,n}$ is the polarizability tensor for the $m \rightarrow n$ transition [6].

$$\left(\sigma_R\right)_{m,n} = \frac{2^7 \pi^5 \nu^4}{3^2 c^4}\left(A_{m,n} + B_{m,n}\right)^2$$

Where $A_{m,n}$ is the diagonal components and $B_{m,n}$ is the off diagonal components of the polarizability tensor. Assuming a single A-term preresonant electronic state $|e\rangle$ and hence only one non-zero element in the polarizability tensor. Then the expression for fundamental scattering is:

$$A_{0,1} = \frac{2e^2}{h^2} M_e{}^2 \langle e|\frac{\partial \hat{H}}{\partial Q_a}|e\rangle\langle 1|Q_a|0\rangle \frac{\nu_e^2 + \nu_0^2}{\left(\nu_e^2 - \nu_0^2\right)^2}$$

Where M_e is the electronic transition length, $\langle e|\frac{\partial \hat{H}}{\partial Q_a}|e\rangle = \hat{H}_{ee}$ is the slope of the excited state potential along the Raman active normal coordinate, ν_0 is the incident frequency, ν_e is the average energy of the excited state $|e\rangle$ and $\langle 1|Q_a|0\rangle$ is a ground state vibrational matrix element of the a[th] normal coordinate [6].

$$A_{0,1}^2 = \frac{2^2 e^4}{h^4} M_e{}^4 \hat{H}_{ee}^2 \left|\langle 1|Q_a|0\rangle\right|^2 \left(\frac{\nu_e^2 + \nu_0^2}{\left(\nu_e^2 - \nu_0^2\right)^2}\right)^2$$

Returning to the scattering cross section $\left(\sigma_R\right)_{m,n}$ expression:

$$\left(\sigma_R\right)_{m,n} = \frac{2^7 \pi^5 \nu^4}{3^2 c^4}\left(A_{m,n} + B_{m,n}\right)^2$$

$B_{m,n} = 0$ as we assume only a single non-zero element in the polarizability tensor. Substituting in for the $A_{0,1}$ term:

$$\left(\sigma_R\right)_{m,n} = \frac{2^9 \pi^5 e^4}{3^2 h^4 c^4} M_e{}^4 \hat{H}_{ee}^2 \left|\langle 1|Q_a|0\rangle\right|^2 \nu^4 \left(\frac{\nu_e^2 + \nu_0^2}{\left(\nu_e^2 - \nu_0^2\right)^2}\right)^2$$

$$\left(\sigma_R\right)_{m,n} = \frac{2^9 \pi^5 e^4}{3^2 h^4 c^4} M_e{}^4 \hat{H}_{ee}^2 \left|\langle 1|Q_a|0\rangle\right|^2 F_A\left(\nu_0\right)^2$$

Where $\boxed{F_A = \nu^2 \left(\frac{\nu_e^2 + \nu_0^2}{\left(\nu_e^2 - \nu_0^2\right)^2} \right)}$ is the dimensionless frequency factor.

Finally

$$\boxed{\left(\sigma_R\right)_{m,n} = KF_A\left(\nu_0\right)^2}$$

Where $K = \frac{2^9 \pi^5 e^4}{3^2 h^4 c^4} M_e{}^4 \hat{H}_{ee}^2 \left|\langle 1|Q_a|0\rangle\right|^2$ is the coupling strength [6].

1.7 Wavelength dependent intensity corrections

The experimental Raman data collected by the spectrograph must be corrected to account for the efficiency of the collecting optics. This correction can be done simply by measuring the spectrum of a standard lamp with a known spectral distribution [5]. The standard lamp used was a white light source and the experimental spectrum of the white light source was compared to its known spectrum. The following equation was used to do the wavelength dependent correction:

$$I_{corrected} = \lambda^2 \left(\frac{I_{known}}{I_{experimental}} \right) I_{uncorrected}$$

Where I_{known} is the known spectral distribution of the lamp, $I_{experimental}$ is the experimental distribution of the lamp, λ is the wavelength, $I_{uncorrected}$ is the uncorrected raw Raman data with the background subtracted off and $I_{corrected}$ is the wavelength dependent corrected experimental Raman intensity.

1.8 Ionic Liquids

Room temperature ionic liquids (RTIL) are liquids that are comprised entirely of ions that are fluid below 100 ºC. Ionic liquids are also known as low, ambient, or room temperature molten salts; ionic fluids; liquid organic salts; fused salts or neoteric solvents. The exact date of the discovery of the first ionic liquid is disputed. However, one of the earlier known ionic liquids synthesised was $[EtNH_3^+][NO_3^-]$ (m.p. 12 °C), which was published in 1914 [7-9]. Ionic liquids are part of a Green Chemistry movement aimed at reducing the amount of volatile organic compounds (VOC's) being released into the environment. Strategies to remove or reduce solvent waste from chemical industries include solvent free synthesis (heterogenous catalysis), non harmful solvents like water, supercritical fluids or ionic liquids. These different methods complement rather than compete with each other. There are at least a million simple ionic liquids possible [7].

Ionic liquids have a range of physical properties that make them suitable for alternatives to traditional organic solvents. Ionic liquids with fully quaternarised nitrogen cations have the common properties of being non-flammable and have negligably low vapour pressure. Negligible vapour pressure means that these liquids do not evaporate. In addition to being a possible green substitute to VOC's, ionic liquids are also being designed to increase reaction rates, specificity and yield [7]. However, some families of ionic liquids can generate an appreciable vapour pressure by distillation under vacuum at 200-300 ºC. This allows the purification and distillations of these ionic liquids [7].

In this thesis the following neat ionic liquids were investigated:

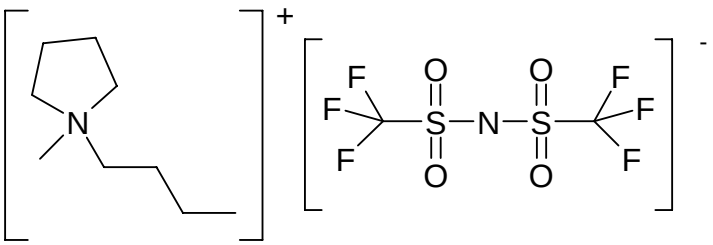

$[CH_3N(C_4H_8)Bu][(F_3CSO_2)_2N]$

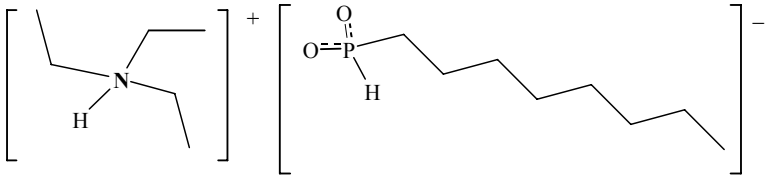

[Et_3NH][(octyl)PO_2H]

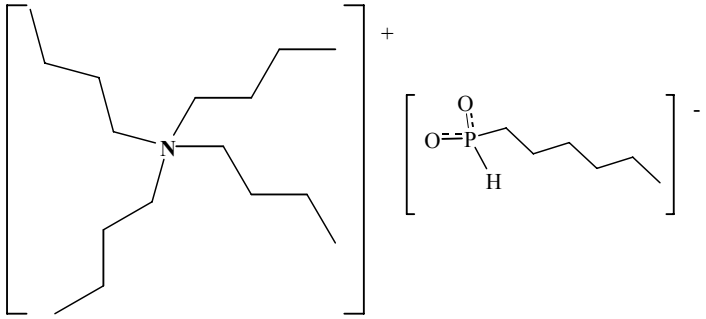

[Bu_4N][(hexyl)PO_2H]

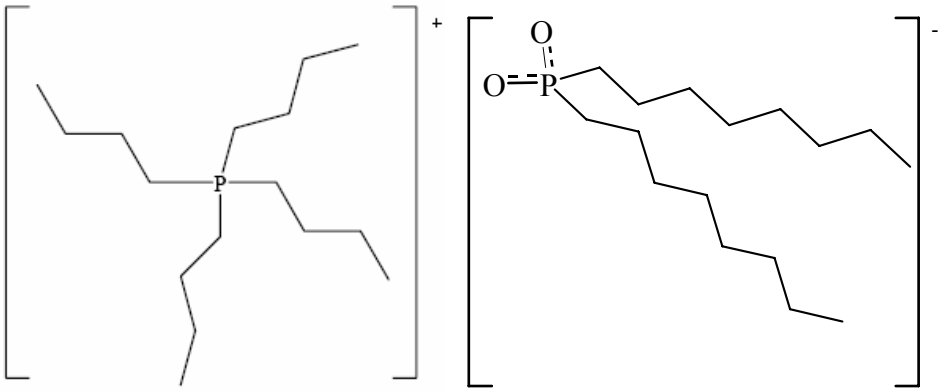

[Bu_4P][$(octyl)_2PO_2$]

The first bistriflimide ionic liquid was kindly provided by Dr Sanjeev Gambhir from the Nanomaterials Research Centre at Massey University, New Zealand; and the other three phosphinate ionic liquids were provided by Professor Bill Henderson of Waikato University, New Zealand.

1.9 Direction of work

Although a number of useful applications for ionic liquids have already been developed, (e.g. dye-sensitised solar cells [10], electroluminescent devices [11] and catalytic reactions [12]) the structure and charge transport processes are only beginning to be understood. For ionic liquids to be considered for use in solar cells we must learn more about the ionic liquid's ability to control interfacial electron-transfer. The flow of electrons can be described by a Marcus-Hush model, which requires an estimate of the solvent reorganisation energy. This may be very different for ionic liquids compared to ordinary liquids. To determine the solvent reorganisation energy of ionic liquids we may use Raman spectroscopy. The first step to doing this is to determine the absolute cross sections of the ionic liquids. Here we present some Raman spectra of ionic liquids and their associated cross sections.

Chapter 2
Experimental

2.0 Experimental Introduction

This chapter is very detailed as the work in this thesis involved the establishment of the Raman apparatus at Massey University, New Zealand. Future publications could refer to this chapter to illustrate the experimental setup and method used.

2.1 Raman Equipment Setup

In order to obtain the differential and absolute cross sections of the ionic liquids, laser light of wavelength 416 nm, 488 nm, 514 nm, 532 nm and 633 nm were scattered off the sample cell. The scattered photons were collected by an Acton Spectra Pro® 2550i, 0.500 m imaging single stage monochromator/spectrograph. The detector was liquid nitrogen cooled to minimise electrical noise.

A vertically polarized Brilliant b, Q-switched Nd: YAG pulse laser (Quantel) operating at 355 nm, 532 nm and 1064 nm was used as the Raman stimulator. Additional wavelengths were obtained by Raman shifting the 532 nm laser line through 80 psi hydrogen gas to give 416 nm. Wavelengths 487 nm and 514 nm were generated by a continuous wave multi-line Stellar-PRO 150 mW Argon laser. The 633 nm light was generated by a continuous wave HeNe laser. The same sample configuration was used for all wavelengths investigated.

2.2 416 nm Raman Experimental Setup

The 416 nm wavelength was the shortest wavelength used after it was found that the spectrograph ordered did not have the required coating to collect light in the UV (355nm) region and that our lenses absorb in this region. The general setup used to obtain the 416 nm wavelength via Simulated Raman Scattering (SRS) from 355 nm is given by Figure 2.1. The second and third harmonic generator was attached to the Nd: YAG laser to provide the 355 nm light.

Figure 2.1: The 416 nm experimental configuration

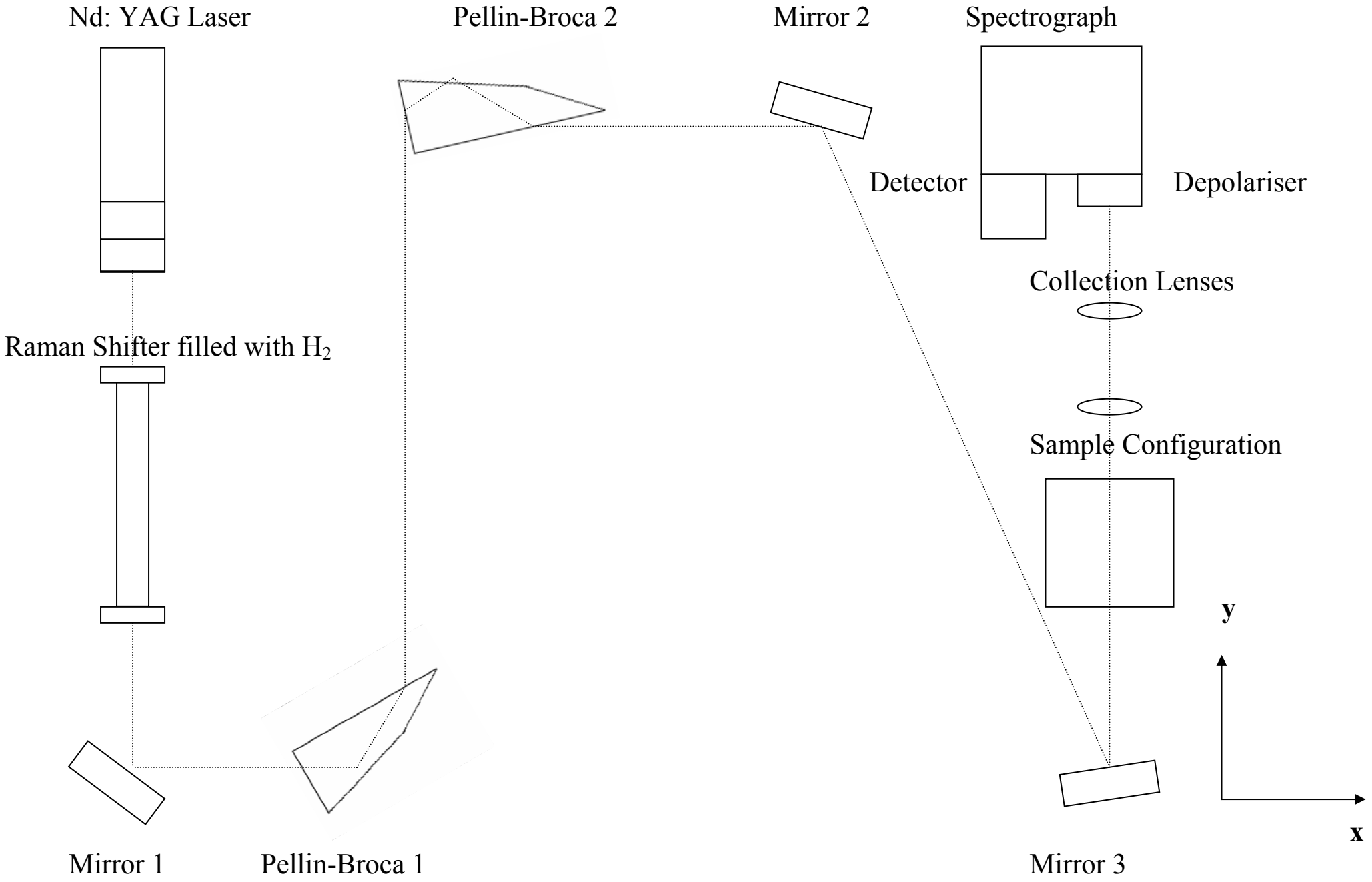

Figure 2.2: Sample configuration for all wavelengths

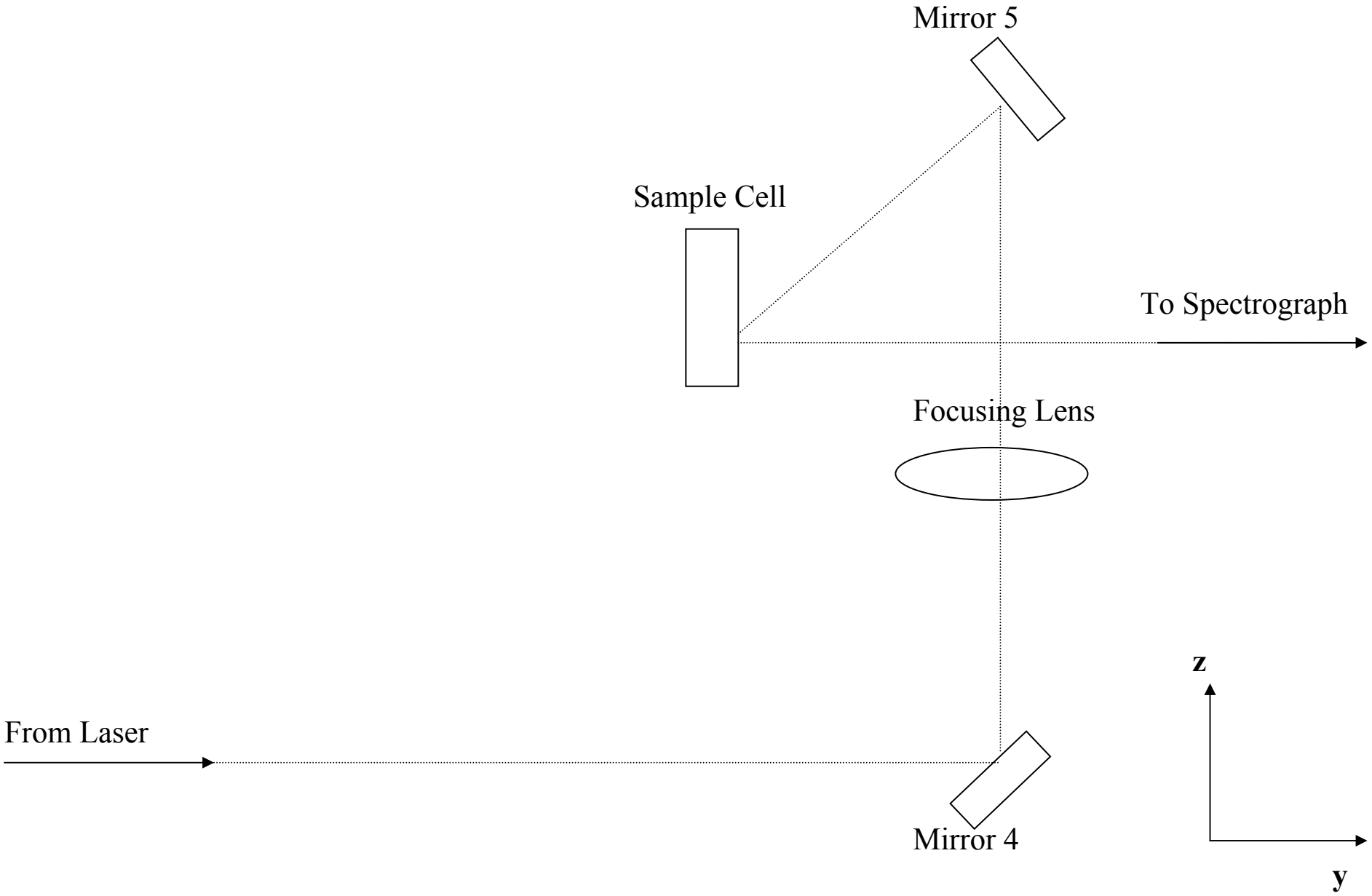

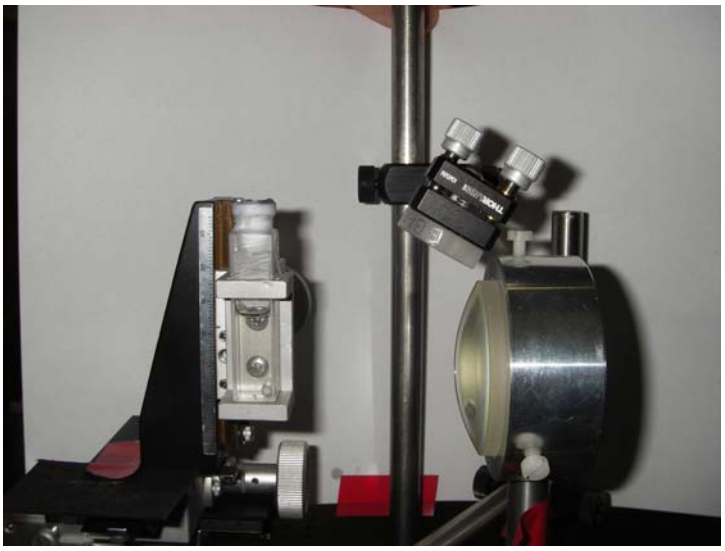

Figure 2.3: The sample configuration used for all wavelengths

Breakdown of equipment used in Figures 2.1 and 2.2

Mirror 1, 2

(BBDS-PM-1037-C) from CVI optics, broadband mirrors 350-1100 nm

Mirror 3, 4, 5

(BB1-E02) from THOR labs, dielectric broadband mirrors 400-750 nm

Pellin-Broca 1, 2

(PLBC-10.0-79.5-UV) from CVI optics, fused silica Pellin-Broca prism

Raman shifter windows

(W1-PW-1025-UV-355-532-0) from CVI optics, fused silica plane wedge, 355 nm and 532 nm anti-reflective coatings

(PW-1025-UV) from CVI optics, fused silica plane window wedge

Raman shifter lenses

(LB4837) from THOR labs, fused silica f = 250 mm

Raman shifter metal tubing

Length = 40 cm

Diameter =5 cm

Sample focussing lens

(LB4282) from THOR labs, fused silica f = 200 mm

Cells

(3/GL14/S) SOG 10 mm, Starna, special optical glass 320-2500 nm

Collection lenses

Achromatic doublet, AC254-150 A1 from THOR labs 400-700 nm, f = 75 mm

Biconvex 2", LB1374-A from THOR labs, f=150 mm

Note: The same collection lenses were used for all the wavelengths.

Figure 2.4: SRS generated 416 nm light illuminating an Ionic Liquid sample.

The focal point of the focusing lens was set to be behind the sample cell for the YAG wavelength of 532 nm and to the centre of the cell for all other wavelengths investigated; this was to prevent degradation of the glass cell by the pulsed laser. The Raman shifter tube had the faces of the tube angled down to prevent reflections off the windows going back into the laser cavity. In addition, the windows had a 355 nm and 532 nm anti-reflective coating. Hollowed foam packaging material was found to make an effective safe beam dump of reflected light. To fill the Raman shifter tube the tube was first evacuated by a vacuum line for 30 minutes then back filled with hydrogen gas to 80 psi. The gas could be held for a maximum of a week, after which a fresh H_2 fill was needed and the procedure was repeated. The 355 nm laser light emitted from the YAG laser was focused to the centre of the Raman shifter tube filled with 80 psi of H_2 gas. The H_2 gas underwent stimulated Raman scattering and the 416 nm light was emitted collinearly with other undesirable wavelengths. To separate the SRS collinear light two Pellin-Broca prisms were used. It was found that when only one Pellin-Broca was used the wavelengths were insufficiently separated, so a second was introduced. An iris could be used for the final separation before the sample configuration to pick off the wavelength of interest.

High damage threshold Broadband mirrors (350-1100 nm) were used as the first two mirrors to prevent mirror degradation as a large amount of 355 nm light, typically 1 watt, was needed to generate the SRS wavelength of 416 nm. As with all Raman scattering most of the light is in the non-Raman/Rayleigh scattered form. After the first Pellin-Broca the 355 nm light was dumped as it did not hit the second Pellin-Broca. Because of the greatly reduced light power, dielectric broadband mirrors (400-750 nm) could be used as mirrors beyond this point.

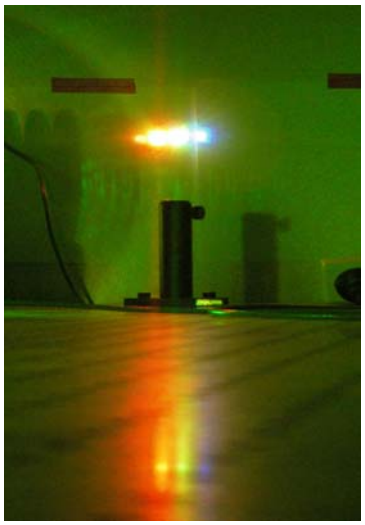

Figure 2.5: SRS Light separation after passing though one Pellin-Broca.

2.3 487 nm and 514 nm Raman Experimental Setup

The 487 nm and 514 nm wavelengths were generated by a multi-line Argon laser. As it was a multi-line laser all the wavelengths were emitted collinearly and Pellin-Brocas were used to separate the wavelengths. The equipment was set up as illustrated in Figure 2.8. Both the 487 nm and 514 nm experimental setups were identical. The 487 nm light was passed though the 487 nm line-pass filter before irradiating the sample. Similarly, the 514 nm light was passed through a 514 nm line-pass filter before irradiating the sample. To change between the 487 nm and 514 nm wavelengths the second Pellin-Broca was simply rotated. This allowed the 514 nm light to be picked off by an iris and passed though the 514 nm line-pass filter.

Figure 2.6: The multi-line argon laser and the first Pellin-Broca setup.

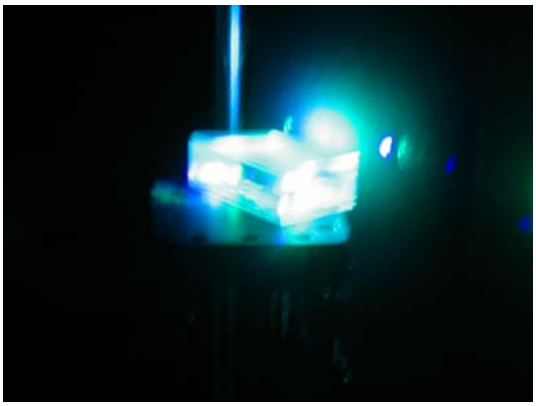

Figure 2.7: Colours a plentiful – the second Pellin-Broca hard at work separating the light from the argon laser.

Figure 2.8: The 487 nm and 514 nm experimental configuration

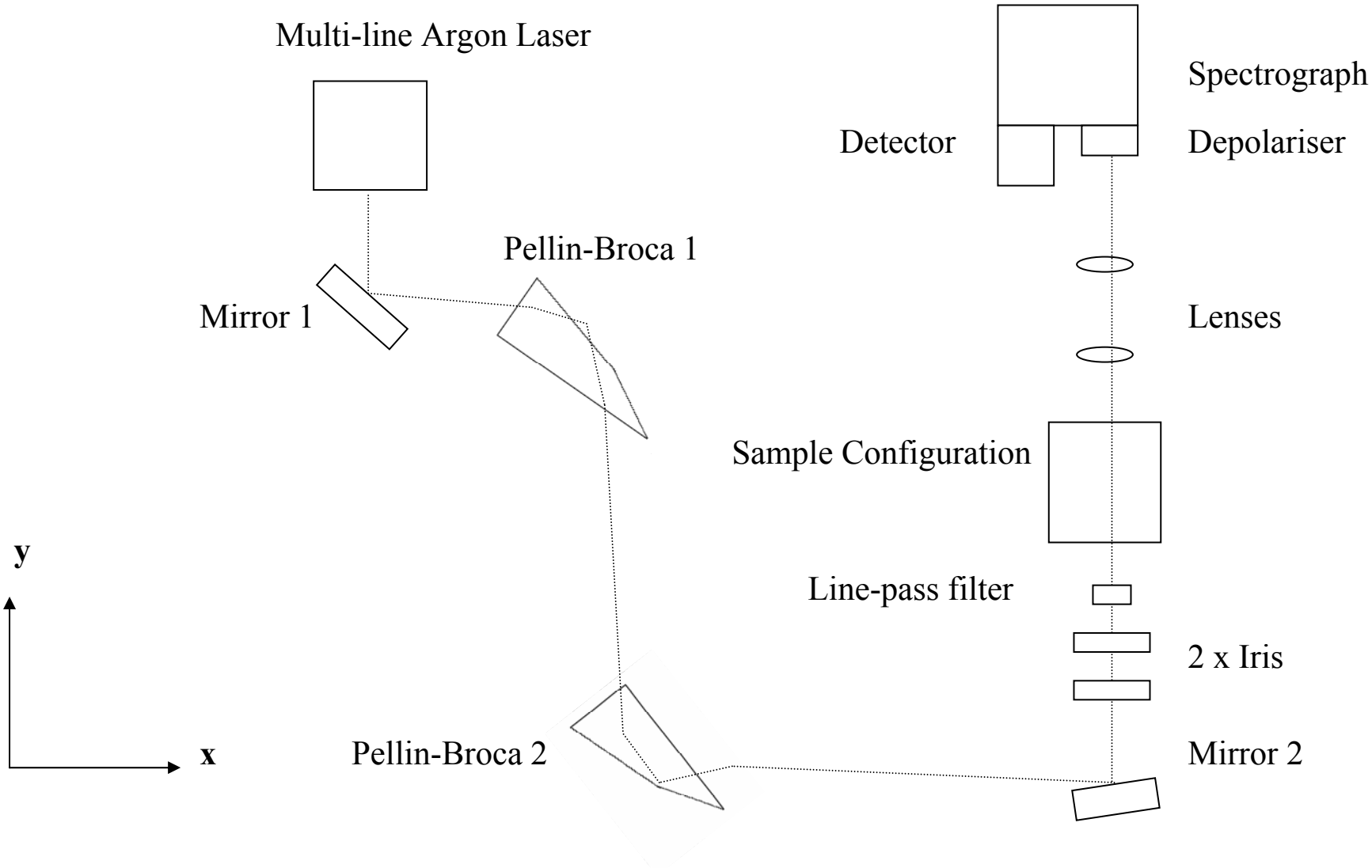

Two irises were used to ensure that the beam entering the sample configuration was in line with the spectrograph. This greatly aided alignment for maximum Raman scattering collection.

Breakdown of equipment used in Figures 2.8

Mirror 1, 2

(BB1-E02) from THOR, dielectric broadband mirrors 400-750nm

Pellin-Broca 1, 2

(PLBC-10.0-79.5-UV) from CVI, fused silica Pellin-Broca prism

Sample lens

(LB4282) from THOR, fused silica f = 200mm

2.4 532 nm Raman Experimental Setup

The 532 nm light was generated from the YAG pulse laser. As no other wavelengths were collinear with the 532 nm light, Pellin-Brocas were not needed to separate the light. The equipment was setup as illustrated in Figure 2.10.

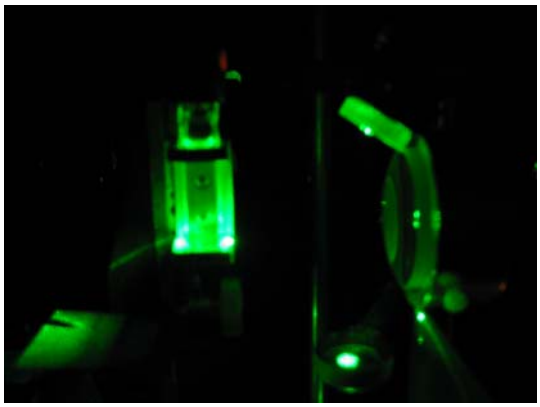

Figure 2.9: A pulse of 532 nm light from the YAG pulse laser illuminating a sample.

Figure 2.10: The 532 nm experimental configuration

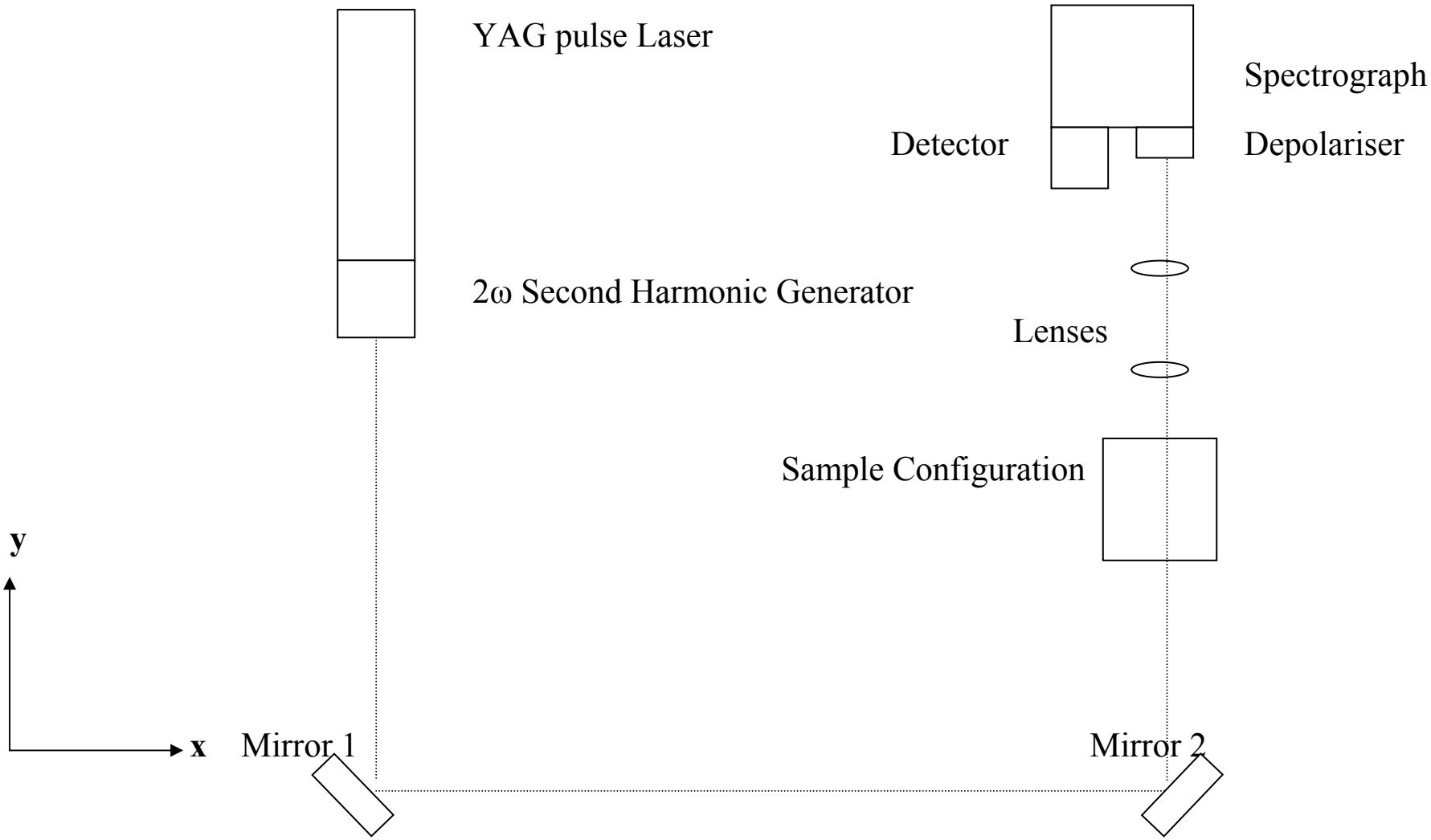

Breakdown of equipment used in Figures 2.10

Mirror 1, 2

(BB1-E02) from THOR, dielectric broadband mirrors 400-750 nm

2ω Second Harmonic Generator

Potassium Dihydrogen Phosphate crystal used to generate the 532 nm light

2.5 633 nm Raman Experimental Setup

The light in the red region was generated by a 633 nm HeNe laser. No additional light was emitted collinearly so no Pellin-Broca was needed. The equipment for the 633 nm experiment was set up as illustrated in Figure 2.12.

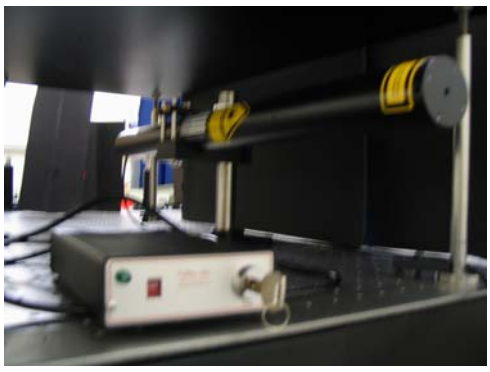

Figure 2.11: The HeNe laser used for generating 633 nm light.

Figure 2.12: The 633 nm experimental configuration

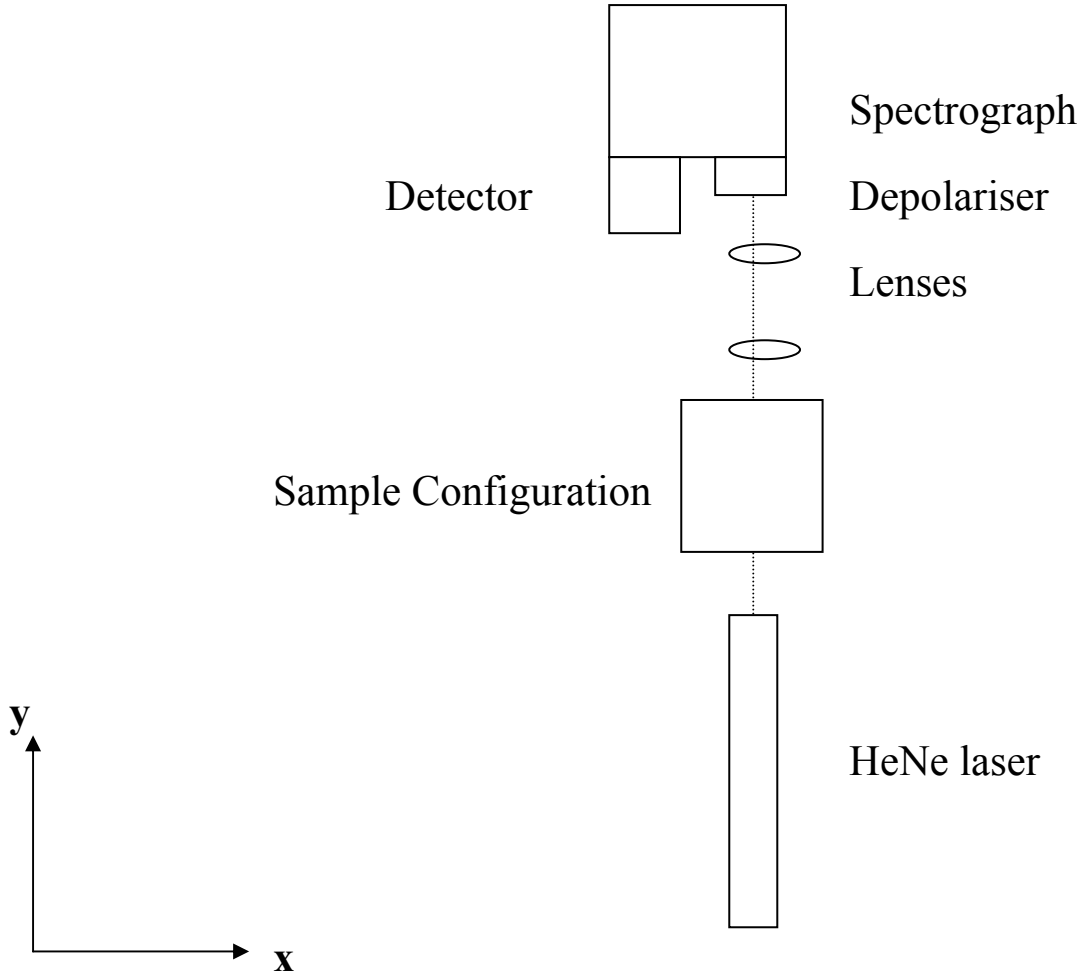

2.6 Depolarization ratio experiments

The depolarisation ratios were collected for all wavelengths for every window used. The setup was the same as given for the collection of the initial Raman spectrum, except that a polariser was placed before the entrance setup of the spectrograph. The polariser could be set to pass either vertically polarised light or horizontally polarised light.

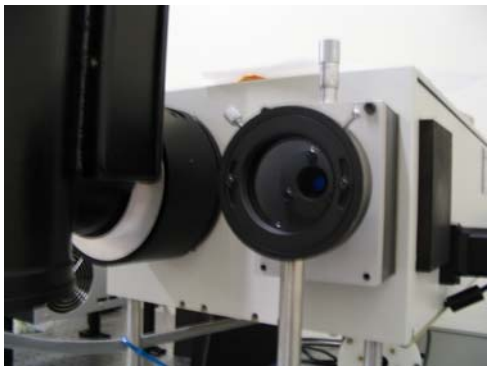

Figure 2.13: The polariser that was situated directly before the entrance setup to the spectrograph.

2.7 Frequency Calibration

The McCreery standard is a 50/50 v/v mix of toluene and acetonitrile and was used as the known standard for calibrating windows of the data collected. The McCreery standard was collected for 12 seconds with 12 repeat accumulations of the collection to allow a very good signal to noise ratio. The experimental peaks of the standard were then assigned using the standard published by Richard L. McCreery from Ohio State University. Each time the spectrograph window was moved or 24 hours elapsed a new calibration had to made.

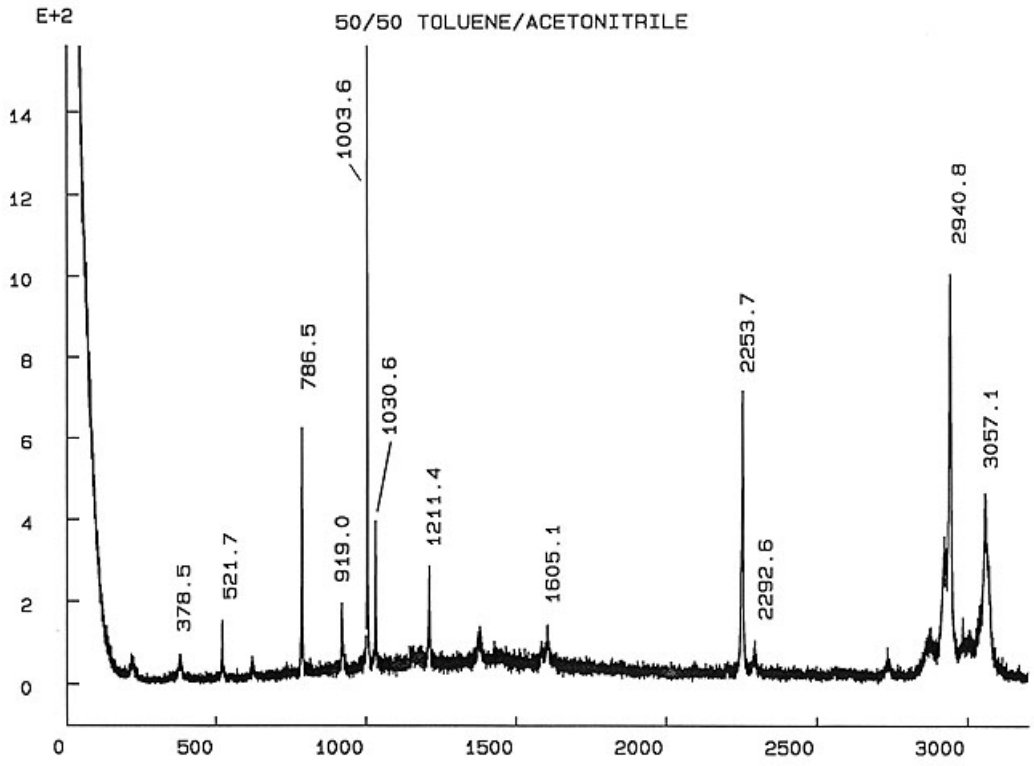

Figure 2.14: Richard L. McCreery's standard of Ohio State University [13].

2.8 The spectrograph window

The entire Raman spectrum could not be collected in a single window. To obtain the entire spectrum the spectrograph position was moved in increments, ensuring good overlap with the previous window. Together the windows would provide the entire Raman spectrum. The spectrograph disperses linearly with wavelength. The reciprocal relationship between wavenumber, and therefore Raman shift, mean that fewer wavenumbers fit in a window at longer wavelength. The 416 nm spectrum was collected in 3 windows; 487 nm and 514 nm in 4 windows; 532 nm in 6 windows and 633 nm in numerous windows. To get around the problem of needing numerous windows the 1200 g/mm grating was used instead of the normal 1800 g/mm grating. This reduced the sharpness of the peaks but allowed the collection of the entire spectrum in 3 windows.

2.9 Beam dumping

After passing through the Raman shifter tube only a very small fraction of light would be the desired SRS light, the rest would be the 355 nm or 532 nm incident light. To remove the undesired light 355 nm or 532 nm dichroic mirrors were used. The 532 nm dichroic mirror would reflect the 532 nm light into a beam dump, while allowing all other wavelengths to pass.

Figure 2.15: The setup of the 532 nm beam dump. SRS light would pass though the dichroic mirror while the 532 nm irradiating light would be reflected into the beam dump.

It was found that by using a Pellin-Broca, the 355 nm light could be separated sufficiently to miss the second Pellin-Broca and dump the light without using a dichroic mirror. The SRS of 532 nm light to give 682 nm light was investigated and the beam dump was used. However, it was found that insufficient 682 nm light could be generated to get appreciable Raman scattering at the sample. This method was abandoned and a 633nm HeNe laser was purchased to give the red light instead.

2.10 Depolariser

A depolarizer is used just before the light enters the spectrograph. This is to scramble the incoming lights polarization to eliminate the problem that the spectrograph might be more sensitive to certain polarisations.

Figure 2.16: The depolariser that is situated in front of the filter and spectrograph entrance slit.

2.11 Laser light filters

As Raman scattering is weak it is dominated by Rayleigh scattering and cannot be observed close to the Rayleigh line. To allow collection of Raman scattering close to the Rayleigh line: notch, long-pass edge and line-pass filters were used. The notch and long-pass edge filters were placed behind the depolariser just before the light entered the spectrograph slit. The line-pass filters were placed just before the sample was illuminated. For 416 nm no filter was used as there were numerous other non-Raman lines close to the laser line that would have saturated the weak Raman lines anyway. For 487 nm an Iridian long-pass filter (PN-ZX000453-002-12-04) was used, for 514 nm an Iridian notch filter (PN-ZX000514-001) was used, for 532 nm an Iridian edge filter was used and for 633 nm an Iridian long-pass filter (PN-ZX000227-002-12A-01) was used.

Notch filters absorb light over a short wavelength range and are ideal for removing the sharp Rayleigh line, edge filters pass light after a cut-off wavelength and long-pass edge filters pass light of longer wavelength above the cut-off wavelength. Conversely, short pass edge filters pass light of shorter wavelength below the cut-off wavelength. Long-pass edge filters were useable in this experiment as we were not interested in anti-Stokes scattering that occurs on the shorter wavelength side of the laser line. Line-pass filters pass light over a very short wavelength, and are ideal for removing unwanted lines from the laser line before the sample is illuminated. Line-pass filters were used for the wavelengths generated from the Argon laser as other

unwanted lines associated with the other atomic transitions in Argon accompanied the 487 nm and 514 nm lines.

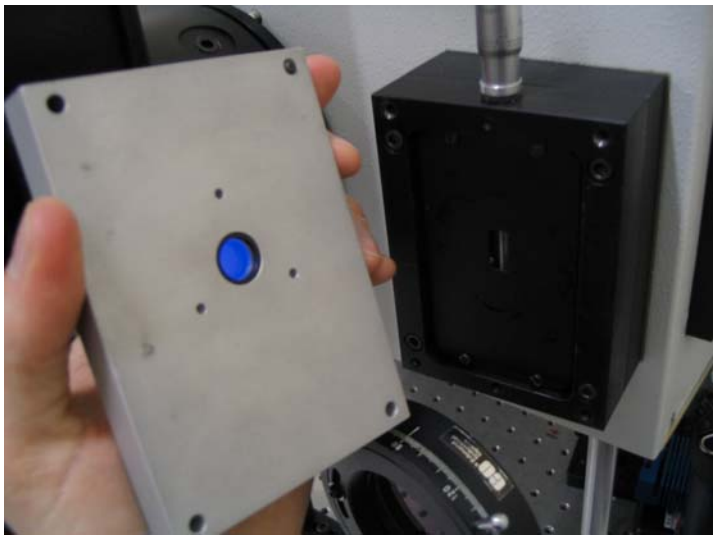

Figure 2.17: A closer look at the 532 nm edge filter behind the depolariser.

2.12 Collection Procedure

The detector was cooled with liquid nitrogen until it had reached its locked temperature as indicated by the computer collection software WinSpec. The equipment was set up as illustrated below for each wavelength.

2.13 416 nm Collection

After the detector had reached the locked temperature the Nd: YAG laser was turned on and allowed to equilibrate with its operational temperature of 35 ºC. The Q-switch could then be operated and the laser could fire. The power meter with a high power threshold was placed directly in front of the YAG laser and the Q-switch was lowered to give maximum power. The dichroic mirrors in the laser could then be tuned to give maximum operational power output. The power meter was then placed directly before the sample configuration with a more sensitive low power threshold head. The Q-switch was set to give approximately 20-30 mW of 416 nm light power to the sample. Powers exceeding 30mW tended to blow chunks out of the sample cell and upset my supervisor.

Windows were chosen such that good overlap of the Raman peaks could be observed between the windows and the spectrograph had the 1800 g/mm grating installed. The McCreery standard was used to calibrate the spectrograph window, the procedure for calibration followed is outlined in the section 2.7. The cell was moved until the position of maximum Raman scattering was found and the spectrograph entrance slit was set to 25 μm to give sharp resolved peaks. The solvents cyclohexane, carbon tetrachloride, acetonitrile and dichloromethane were used as standards with the four ionic liquids. It was found that benzene's 992 rel cm^{-1} mode was very strong for 416 nm and would saturate the spectrograph. To get around this problem acetonitrile was used in its place as a standard for the 416 nm wavelength experiment. The saturation of the strongest band for the solvents in the window was identified and a collection time slightly below this threshold was set. A collection time of 12 seconds was used and averaged with 12 separate accumulations to get a good signal to noise ratio. The samples were run one after the other: cyclohexane, carbon tetrachloride, acetonitrile, dichloromethane and the four ionic liquids. The runs were repeated four times to allow for good statistics. A background and white light collection was made at the end of the four runs. Three windows were collected each having overlapping regions with the previous window. The windows were centred on 442 nm, 458 nm and 470 nm. This procedure was repeated for each new window. The 458 nm window was found to have no Raman active bands and consequently only one run was collected.

2.14 487 nm and 514 nm Collection

After the detector had reached the locked temperature the Argon laser was turned on, set to maximum power and allowed to equilibrate for 20 minutes. The power of the 487 nm or 514 nm light entering the sample configuration was measured by the power meter with a low power threshold. Powers were typically between 20-25 mW depending on how well the optics were aligned. As the laser gave a continuous wave rather than a pulse there was no danger of cells being blown apart and my supervisor could sleep easy. Windows were chosen such that good overlap of the Raman peaks could be observed between the windows, the spectrograph had the 1800 g/mm grating installed and the spectrograph entrance slit was set to 100 μm for both the 487 nm and

514 nm experiments. The McCreery standard was used to calibrate the spectrograph window and the cell position was optimised to allow for the maximum amount of Raman scattered light to be collected the spectrograph. The solvents cyclohexane, carbon tetrachloride, benzene and dichloromethane were used as standards with the four ionic liquids. The saturation of the strongest band for the solvents in the window was identified and a collection time slightly below this threshold was set. A collection time of 8 seconds was averaged with 15 separate accumulations to get a good signal to noise ratio for the 487 nm experiment and a collection time of 12 seconds was averaged with 12 separate accumulations to get a good signal to noise ratio for the 514nm experiment. The samples were run one after the other: cyclohexane, carbon tetrachloride, benzene, dichloromethane and the four ionic liquids. The runs were repeated four times to allow for good statistics and a background and white light collection was made at the end of the four runs. Four windows were collected each with overlapping regions with the previous window. The windows for the 487 nm experiment were centred on 504 nm, 514 nm, 528 nm and 565 nm; and the windows for the 514 nm experiment were centred on 531 nm, 538 nm, 557 nm and 603 nm. The procedure was repeated for each new window.

2.15 532 nm Collection

After the detector had reached the locked temperature the YAG laser was turned on and allowed to equilibrate with its operational temperature of 35 ºC. The Q-switch could then be operated and the laser could fire. The power entering the sample configuration was measured using a low power threshold power meter and the power was set to 25-30 mW. The cell position was optimised to allow for the maximum amount of Raman scattered light to be collected the by spectrograph. The saturation of the strongest band for the solvents in the window was identified and a collection time slightly below this threshold was set. Windows were chosen such that good overlap of the Raman peaks could be observed between the windows, the spectrograph had the 1800 g/mm grating installed, the McCreery standard was used to calibrate the spectrograph window and the spectrograph entrance slit was set to 50 μm to give sharp resolved peaks. The solvents cyclohexane, carbon tetrachloride, benzene and dichloromethane were used as standards with the four ionic liquids. A collection time

of 6 seconds was used and averaged with 12 separate accumulations to get a good signal to noise ratio. The samples were run one after the other: cyclohexane, carbon tetrachloride, acetonitrile, dichloromethane and the four ionic liquids. The runs were repeated four times to allow for good statistics and a background and white light collection was made at the end of the four runs. Six windows were collected each with overlapping regions with the previous window. The windows were centred on 545 nm, 565 nm, 580 nm, 596 nm, 613 nm and 613 nm. The procedure was repeated for each new window.

2.16 633 nm Collection

After the detector had reached the locked temperature the 633 nm HeNe laser was turned on and allowed to equilibrate for an hour. The power entering the sample configuration was measured with a low power threshold power meter. There was no control available to vary the power output of the HeNe laser. Typically the power reaching the sample configuration was between 18-20 mW. The light was both low power and continuous wave, meaning that there was no danger of damage. The cell position was optimised to allow for the maximum amount of Raman scattered light to be collected the by spectrograph. The saturation of the strongest band for the solvents in the window was identified and a collection time slightly below this threshold was set. Windows were chosen such that good overlap of the Raman peaks could be observed between the windows, the spectrograph had the 1200 g/mm grating installed whereas the previous wavelengths investigated used the 1800 g/mm grating, the McCreery standard was used to calibrate the spectrograph window and the spectrograph entrance slit was set to 100 μm. The solvents cyclohexane, carbon tetrachloride, benzene and dichloromethane were used as standards with the four ionic liquids. A collection time of 8 seconds was used and averaged with 15 separate accumulations to get a good signal to noise ratio. The samples were run one after the other: cyclohexane, carbon tetrachloride, acetonitrile, dichloromethane and the four ionic liquids. The runs were repeated four times to allow for good statistics and a background and white light collection was made at the end of the four runs. Three windows were collected each with overlapping regions with the previous window.

The windows were centred on 660 nm, 685 nm and 770 nm. The procedure was repeated for each new window.

2.17 Background collection

For every window of data collected a background spectrum was collected to compensate for background light in the laser laboratory. This was done by removing the cell and collecting data for the same time period as for the samples. If a cosmic event (which gives a sharp strong line in the spectrum) had been recorded in the collection the background was collected again until a clean background was recorded.

2.18 White light collection

To determine the spectrograph's response to light a white light source was used. The light was placed in place of a sample and illuminated the spectrograph entrance, turned on and left to equilibrate for 10 minutes, attenuated by placing tissues in front of the entrance slit and collected for 10 seconds with 6 repeat accumulations to give a good signal to noise ratio.

2.19 Polarisation collection

Polarisation data was collected for every window of data. The same start up procedure was followed as for each of the wavelengths except that a polariser was introduced just before the spectrograph entrance. Both the vertical and horizontal polarisations of the standards and samples used were collected. The samples were collected for the same time period as the other Raman data except that only one run of data was collected. The background was recorded for both the vertical and horizontal polarisations using the same method as outlined in section 2.17. The white light spectrum was not needed as we were interested in the ratios of the horizontal to vertical spectrums rather than comparing to other peaks.

2.20 Laser wavelength determination

The Rayleigh line of the scattered light was determined by calibrating the window of which the light appeared in with an Argon lamp. Saturation of the spectrograph by the Rayleigh line was avoided by placing tissues over the entrance slit to attenuate the light entering the spectrograph. Our results were comparable with the manufacturer's specifications.

2.21 Infrared experimental collection

To accompany the Raman data, infrared data was also collected. The infrared data was collected using a Nicolet 5700 FT-IR instrument from Thermo Electron Corporation. Infrared spectra of the four ionic liquids were collected for the neat liquids. The infrared spectrometer had a custom built chamber that could flush the sample with nitrogen gas during data collection. Each sample was flushed with nitrogen gas for five minutes then an 80 second acquisition time and was run. The background was automatically subtracted off with new background data being recorded every 30 minutes to account for background changes over time.

Chapter 3
Gaussian Calculations

3.0 Gaussian Calculations Introduction

Gaussian calculations were run to aid with the band assignments and to get calculated Raman spectra of the ionic liquids to compare with experimental data. Calculations were done on single cation or anion molecules in the gas phase without designing complicated models. Higher order models for ionic liquids have already been developed for small complex forming ionic liquids [14]. Calculations could not be performed for the ionic liquid $[CH_3N(C_4H_8)Bu][(F_3CSO_2)_2N]$ as the anion would crash before the calculations could be completed. Higher level calculations and different methods calculations were tried without success. After this thesis was completed Dr Mark Waterland did a series of geometry opimisations and sucessfully carried out a B3LYP 6-31+G(d) calculation on $[(F_3CSO_2)_2N]$, the results of this calcuation is inculded in the appended DVD. These are the first calculations to have ever been done on phosphinate materials.

3.1 Raman Calculations Run

Gaussian® 03W was used to calculate the Raman and infrared vibrational frequencies of the ionic liquids investigated. The calculations were done using the Density Functional Theory (DFT) hybrid method of B3LYP on an individual cation or anion. The individual cation and anion calculations could then be added together give a calculated spectrum of the neat ionic liquid. Basis sets of 6-31G, 6-31+ G, 6-31 (d), 6-31+ G (d) and 6-31G+ (d, p) were used on each cation and anion. Split valence triple zeta basis sets (6-311) were not used as they were found to be computationally expensive and offered little improvement. For calculations involving anions where an electron is delocalized it is important to use diffuse functions like s, p and d. These diffuse functions add an extra s, p or d type orbital to the minimum basis set. The + also refers to diffuse functions, in this case the next orbital above the minimum basis set is included in the calculation. We did not run ++ calculations where diffuse functions are added to light atoms (hydrogen and helium) as they were found to be computationally expensive and offered little improvement [15]. Gaussian® 03W was

used to first do a geometry optimisation then a Raman and infrared frequency calculation. In this section we present only the highest level of calculation. For a full set of the calculations performed see the appended DVD.

3.3 Raman Calculation Results

Table 3.1: Major Raman intensities (predicted intensities greater than 10) for the ionic liquid $[Et_3NH]^+[(octyl)PO_2H]^-$.

Cation		Anion	
B3LYP 6-311G		B3LYP 6-31G+	
Frequency	Raman Intensity	Frequency	Raman Intensity
1351.656	10.841	693.954	25.645
1526.485	16.587	805.735	17.271
1535.402	24.205	897.459	12.393
1536.615	5.819	1082.004	16.964
1539.931	10.969	1235.168	19.662
3044.718	102.154	1490.028	14.865
3072.384	48.254	1522.881	18.271
3077.871	85.765	1526.319	46.933
3088.489	99.415	1535.818	10.987
3101.070	28.811	2018.725	270.897
3103.675	136.631	2992.723	24.608
3111.041	35.498	2997.822	24.261
3113.968	55.433	2998.904	246.868
3117.036	77.724	3000.751	23.944
3120.462	79.795	3007.317	103.816
3148.218	14.427	3025.250	224.638
3403.872	38.376	3031.500	48.750
		3042.075	101.436
		3063.466	21.957
		3072.950	26.059
		3096.085	33.311
		3103.458	31.200

Note: The anion's predicted P-H stretch is shaded. No other bands on the cation or anion are predicted near 2000 rel cm^{-1}.

For a set of band assignments of the ionic liquids see Chapter Four.

The calculated intensities were used as the area of a Lorentzian function for each predicted peak. Experimental widths were used as a guide for the simulated width. The cation and anion predicted spectra were then added to give an estimate of the calculated experimental spectrum. The resulting spectrum is given by Figure 3.1.

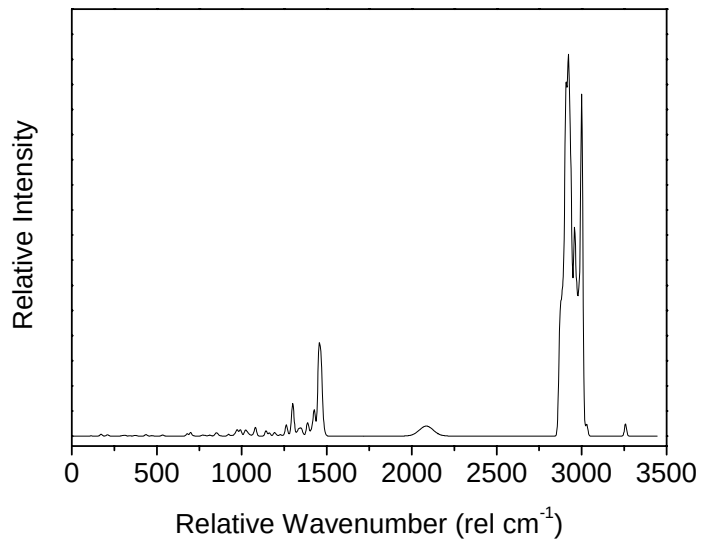

Figure 3.1: The calculated Raman spectrum of the ionic liquid $[Et_3NH]^+[(octyl)PO_2H]^-$.

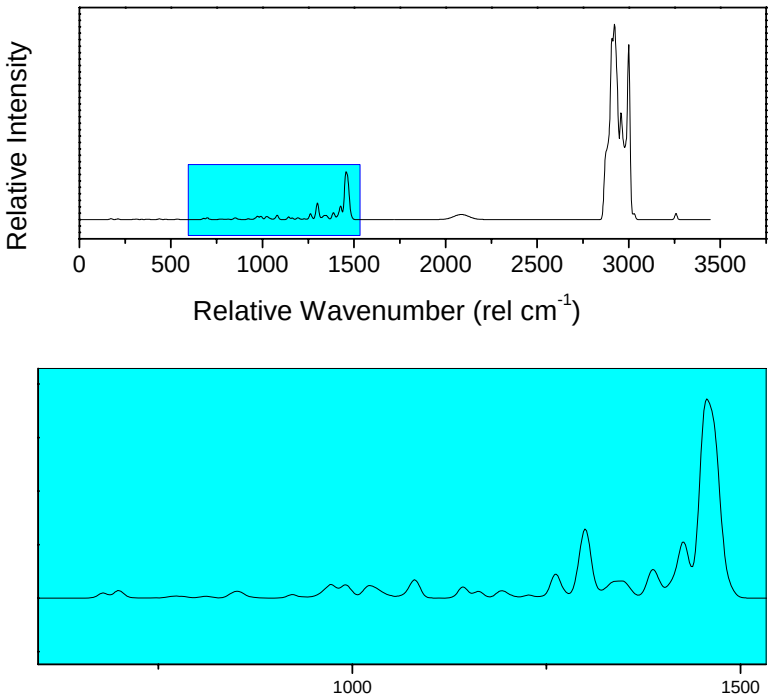

Figure 3.2: A zoom plot of the predicted Raman spectrum for the ionic liquid $[Et_3NH]^+[(octyl)PO_2H]^-$.

The predicted spectrums frequency was multiplied by 0.9571 to allow better agreement with experimental frequencies as DFT calculations slightly overestimate the frequency [16]. A comparison between the predicted and experimental frequencies is given by Table 3.2 and Figure 3.3.

Table 3.2: Comparison between predicted and experimental frequencies.

Predicted Band		Experimental Band		Difference in
Frequency	Relative Intensity	Frequency	Relative Intensity	Frequency Δf
679	0.47	743	4.07	64
699	0.69	763	3.45	64
1081	1.65	1059	10.43	-22
1299	6.44	1304	9.49	5
1425	5.2	1406	4.22	-19
1456	18.59	1455	18.59	-1
2086	1.97	2325 Broad	8.17	239
2922	76.02	2949	60.1	27
2957	41.5	2985	49.25	28
2999	68	3035	17.17	36

Note: The anions P-H stretch is shaded.

The calculations do an adequate job of predicting the bands frequency and intensity above 1000 rel cm^{-1} with the exception of the PH stretch. However, they do not predict the lower frequency bands very well and vastly underestimate the relative intensities. The anion's P-H stretch is very broad and is shifted several orders of magnitude from the calculated position. For more information about the Raman band assignments see Chapter Four.

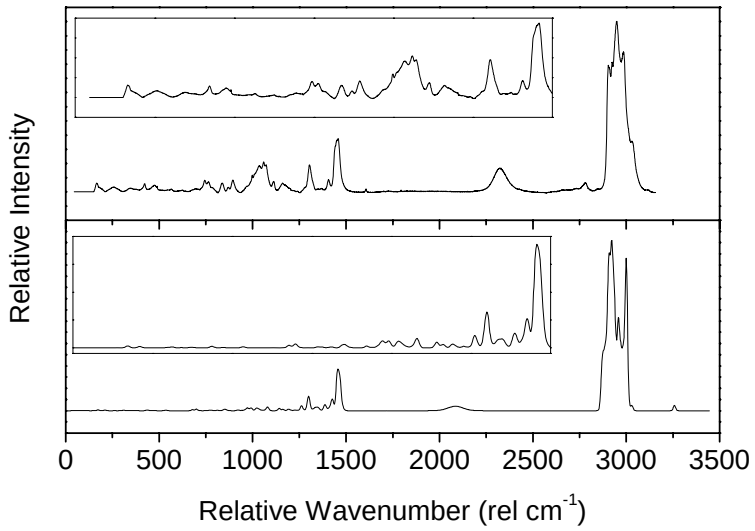

Figure 3.3: The 532 nm experimental Raman spectrum (Top) and the predicted Raman spectrum (Bottom) for the ionic liquid $[Et_3NH]^+[(octyl)PO_2H]^-$.

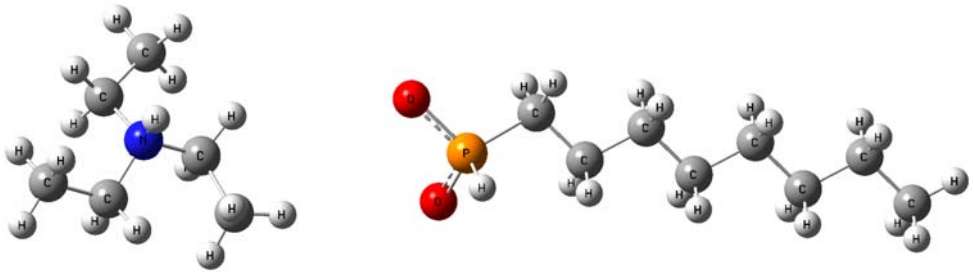

Figure 3.4: The cation and anion of the ionic liquid $[Et_3NH]^+[(octyl)PO_2H]^-$.

Table3.3: Major Raman intensities (predicted intensities greater than 10) for the ionic liquid $[Bu_4N]^+[hexylPO_2H]^-$.

Cation		Anion	
B3LYP 6-31G(d)		B3LYP 6-31G+(d, p)	
Frequency	Raman Intensity	Frequency	Raman Intensity
870.869	14.553	1030.772	19.152
1061.953	12.165	1064.013	13.632
1075.566	10.469	1196.932	13.957
1348.810	14.815	1320.055	14.912
1360.779	17.332	1457.435	11.727
1366.916	10.687	1486.905	18.727
1517.213	27.118	1489.322	16.330
1518.154	23.503	1497.335	13.359
1518.493	19.645	2179.978	209.967
1519.586	17.938	2991.534	66.565
1525.856	31.048	2996.895	13.054
1529.985	28.383	3001.851	177.438
1530.600	10.523	3009.215	53.744
1536.279	19.798	3011.861	110.854
3035.722	85.205	3017.475	95.324
3038.983	92.757	3020.680	238.585
3044.461	75.351	3029.700	30.042
3044.831	181.038	3049.831	93.822
3048.736	33.496	3053.235	10.197
3050.554	50.361	3083.926	128.928
3054.686	68.862	3088.154	34.249
3055.296	57.575		
3088.945	72.726		
3089.433	128.755		
3094.482	20.966		
3095.711	98.723		
3102.668	98.621		
3112.169	10.646		
3118.924	16.063		
3122.556	38.867		

Note: The anion's predicted P-H stretch is shaded. No other bands on the cation or anion are predicted near 2000rel cm^{-1}.

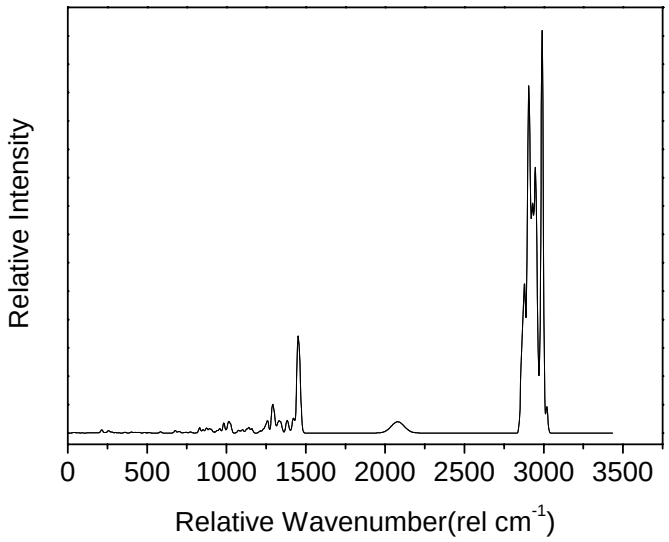

Figure 3.5: The calculated Raman spectrum of the ionic liquid $[Bu_4N]^+[hexylPO_2H]^-$.

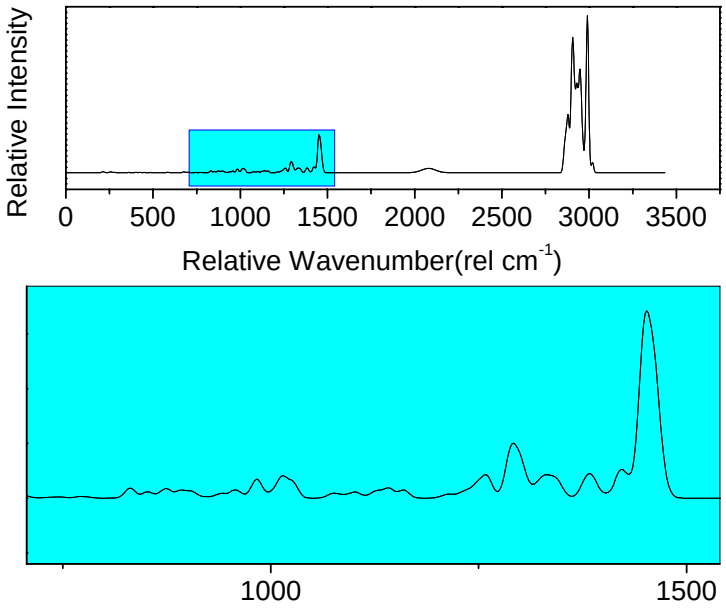

Figure 3.6: A zoom plot of the predicted Raman spectrum for the ionic liquid $[Bu_4N]^+[hexylPO_2H]^-$.

The predicted spectrum's frequency was multiplied by 0.9540 to allow better agreement with experimental frequencies [16]. A comparison between the predicted and experimental frequencies is given by Table 3.4 and Figure 3.7.

Table 3.4: Comparison between predicted and experimental frequencies.

Predicted Band		Experimental Band		Difference in
Frequency	Relative Intensity	Frequency	Relative Intensity	Frequency Δf
982	1.72	903	5.79	-79
1015	2.03	1050	8.35	35
1332	2.1	1323	5	-9
1420	2.6	1409	1.18	-11
1451	17.11	1452	10.56	1
2079	1.97	2252	2.1	173
2905	61.18	2925	30	20
2947	46	2969	29	22
2988	69	2986	30	-2
3019	4.64	3010	20.3	-9

Note: The anion's P-H stretch is shaded.

The calculations do a good job of predicting the bands frequency and intensity above 1000 rel cm^{-1} with the exception of the PH stretch. However, they do not predict the lower frequency bands very well and underestimate the relative intensities. The anion's P-H stretch is very broad and is also shifted several orders of magnitude from the calculated position. For more information about the Raman band assignments see Chapter Four.

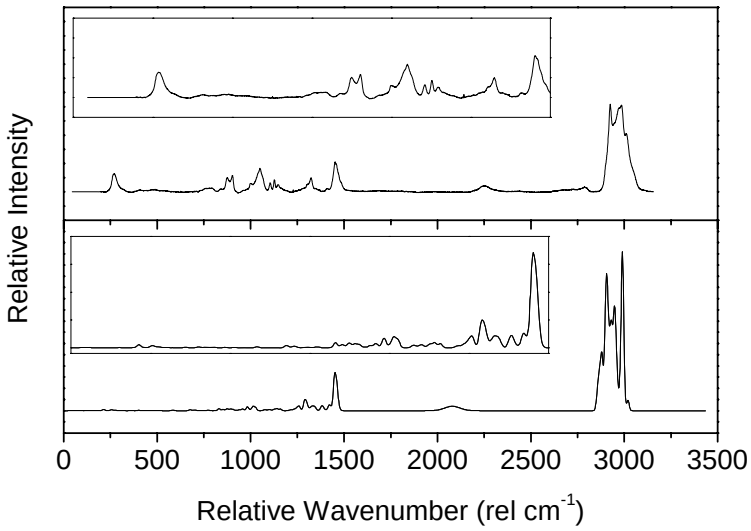

Figure 3.7: The 532 nm experimental Raman spectrum (Top) and the predicted Raman spectrum (Bottom) for the ionic liquid $[Bu_4N]^+[hexylPO_2H]^-$.

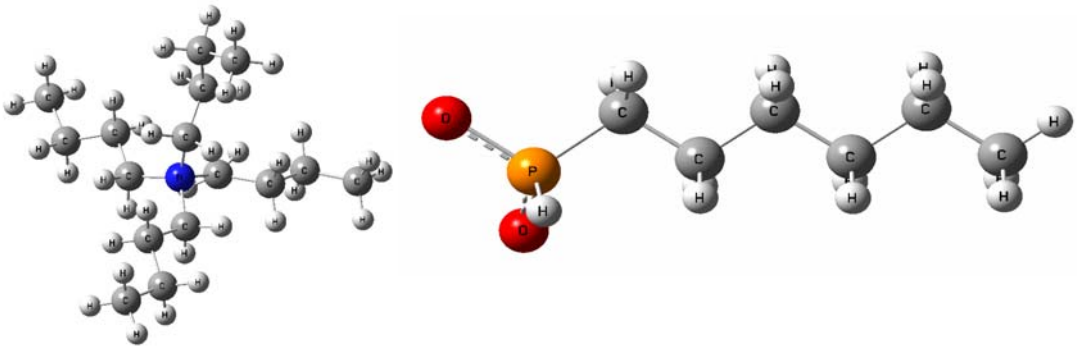

Figure 3.8: The cation and anion of the ionic liquid $[Bu_4N]^+[hexylPO_2H]^-$.

Table 3.5: Major Raman intensities (predicted intensities greater than 10) for the ionic liquid $[Bu_4P]^+[(octyl)_2PO_2]^-$.

Cation		Anion	
B3LYP 6-31G(d)		B3LYP 6-31G+(d)	
Frequency	Raman Intensity	Frequency	Raman Intensity
664.0297	11.6844	686.8787	15.7348
905.3344	12.0123	1010.034	13.2018
914.7915	10.6284	1031.033	15.6248
919.4499	10.4588	1076.489	26.8705
1060.587	13.0088	1193.824	15.4844
1129.942	14.8328	1226.544	14.3358
1358.105	37.8117	1328.382	17.0176
1359.717	30.0162	1328.425	11.0195
1488	10.7195	1331.476	37.2066
1515.678	11.8832	1472.183	10.7721
1517.86	87.3213	1480.908	11.7012
1518.283	25.9578	1504.759	14.9878
1529.947	17.4798	1505.002	15.041
1530.399	22.4155	1507.078	48.6611
1530.944	18.0439	1508.173	36.7528
1531.347	22.3637	1520.751	12.7379
3035.677	19.8004	2992.788	46.4273
3036	50.4004	3000.403	93.0656
3036.189	247.1591	3001.612	13.9312
3051.75	18.6032	3009.059	114.7768
3053.846	23.1986	3012.146	273.4318
3054.054	310.6646	3014.161	229.7676
3054.446	193.7032	3016.713	181.785
3056.319	29.8917	3018.81	68.8455
3062.916	85.6829	3019.006	90.3103
3064.402	105.4708	3025.117	79.8953
3065.481	94.4076	3028.313	427.5745
3065.645	39.5593	3030.122	18.4109
3134.635	103.8489		
3134.741	114.4322		

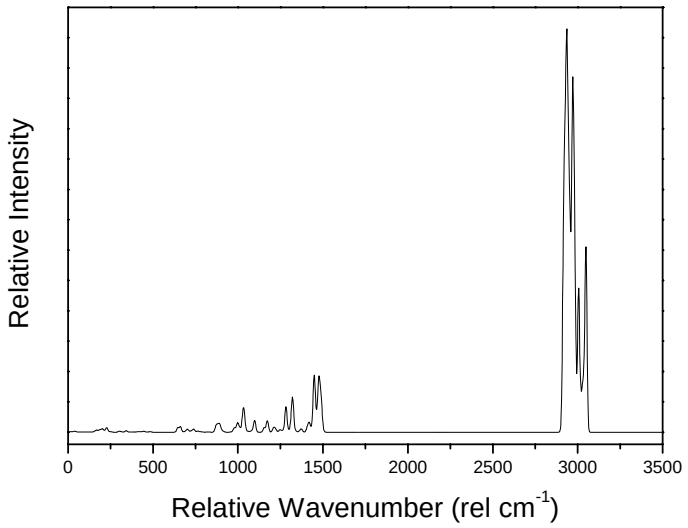

Figure 3.9: The calculated Raman spectrum of the ionic liquid $[Bu_4P]^+[(octyl)_2PO_2]^-$.

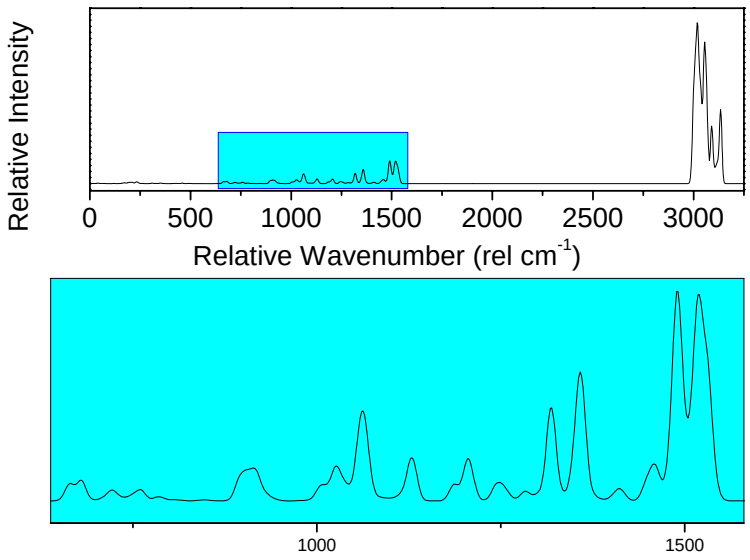

Figure 3.10: A zoom plot of the predicted Raman spectrum for the ionic liquid $[Bu_4P]^+[(octyl)_2PO_2]^-$.

The predicted spectrums frequency was multiplied by 0.9726 to allow better agreement with experimental frequencies [16]. A comparison between the predicted and experimental frequencies is given by Table 3.6 and Figure 3.9.

Table 3.6: Comparison between predicted and experimental frequencies.

Predicted Band		Experimental Band		Difference in
Frequency	Relative Intensity	Frequency	Relative Intensity	Frequency Δf
227	0.74	256	5.8	29
662	0.9	680	3.21	18
887	1.46	888	5.3	1
1320	5.79	1300	5.65	-20
1448	9.4	1410	3.2	-38
1478	9.27	1450	13.5	-28
2935	66.45	2924	42.22	-11
2971	58.54	2951	42.83	-20
2985	34.54	3004	23.76	19
3048	30.54	3010	16.64	-38

The calculations do a good job for predicting most of the band frequencies. The calculations tend to underestimate the relative intensities for higher frequencies and underestimate for lower frequencies. This ionic liquid does not have a P-H group, so the 1500-2750 rel cm^{-1} region is empty.

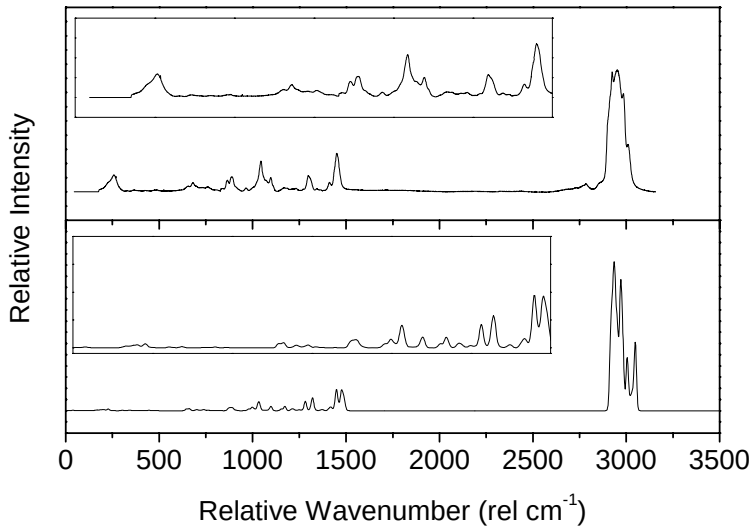

Figure 3.11: The 532 nm experimental Raman spectrum (Top) the predicted Raman spectrum (Bottom) for the ionic liquid $[Bu_4P]^+[(octyl)_2PO_2]^-$.

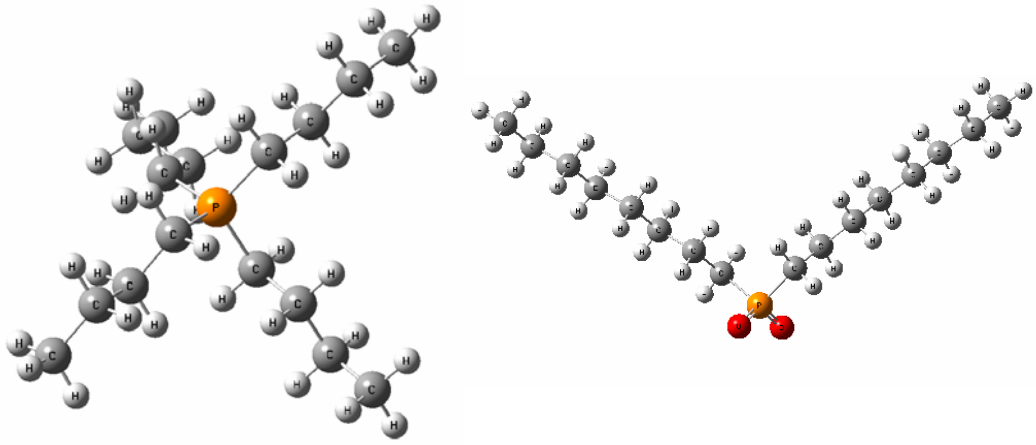

Figure 3.12: The cation and anion of the ionic liquid $[Bu_4P]^+[(octyl)_2PO_2]^-$.

3.4 Infrared Calculation Results

Table 3.7: Major infrared intensities (predicted intensities greater than 10) for the ionic liquid $[Et_3NH]^+[(octyl)PO_2H]^-$.

Cation		Anion	
B3LYP 6-311G		B3LYP 6-31G+	
Frequency	Infrared Intensity	Frequency	Infrared Intensity
802.623	20.557	297.629	13.856
1018.344	10.783	327.168	25.152
1020.756	26.634	363.721	19.800
1030.786	22.904	388.841	15.224
1396.718	12.760	693.954	15.913
1447.897	52.252	742.602	18.420
1469.798	23.259	805.735	81.103
1475.686	16.515	849.364	66.995
1531.457	15.792	897.459	35.731
1535.402	17.023	904.680	34.097
1536.615	16.214	959.715	118.023
1542.390	18.289	979.377	99.684
1551.728	41.940	993.821	40.477
1556.248	10.510	1043.297	17.521
3103.675	10.116	1097.144	15.403
3120.462	10.268	1149.729	10.850
3135.293	15.465	1235.168	24.161
3140.053	11.668	1551.226	14.609
3148.218	10.284	2018.725	440.811
3403.872	19.509	2997.822	10.918
		3007.317	48.270
		3063.466	93.993
		3093.331	65.486
		3096.085	89.842
		3103.458	52.924

Note: The anion's predicted P-H stretch is shaded. No other bands on the cation or anion are predicted near 2000 rel cm^{-1}.

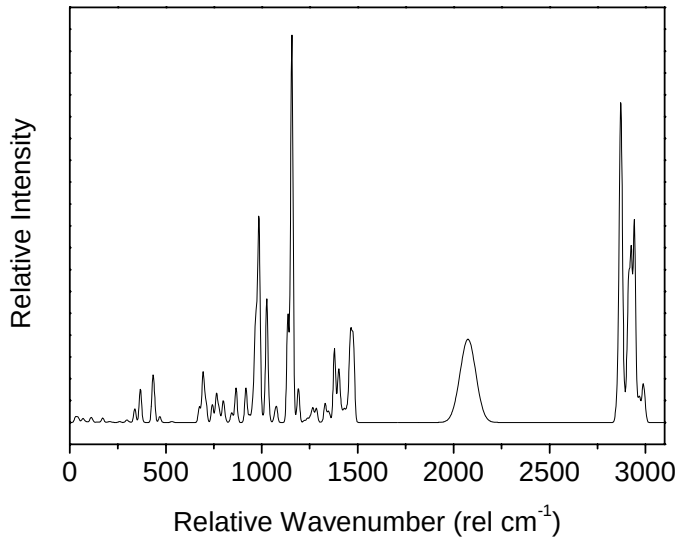

Figure 3.13: The calculated infrared spectrum of the ionic liquid $[Et_3NH]^+[(octyl)PO_2H]^-$.

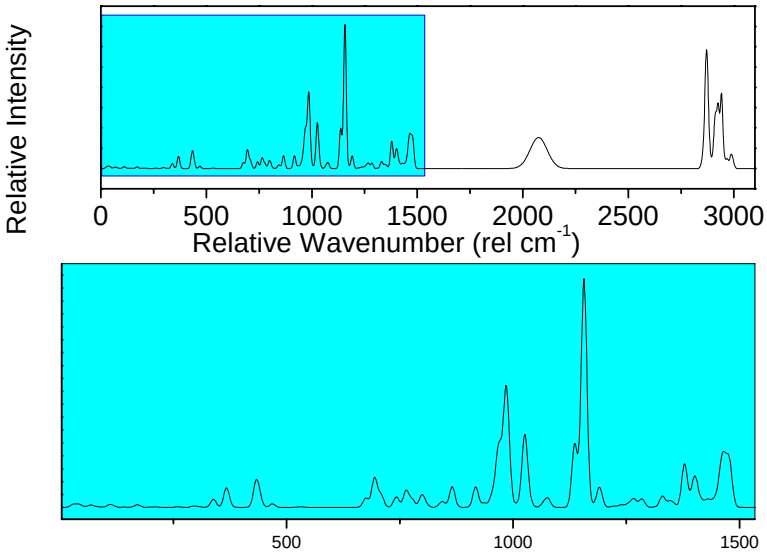

Figure 3.14: A zoom plot of the predicted infrared spectrum for the ionic liquid $[Et_3NH]^+[(octyl)PO_2H]^-$.

The predicted spectrums frequency was multiplied by 0.9571 to allow better agreement with experimental frequencies [16]. A comparison between the predicted and experimental frequencies is given by Table 3.8 and Figure 3.15.

Table 3.8: Comparison between predicted and experimental frequencies.

Predicted Band		Experimental Band		Difference in
Frequency	Relative Intensity	Frequency	Relative Intensity	Frequency Δf
765	1.33	759	1.73	-6
916	1.55	838	1.38	-78
984	9.45	970	5.87	-14
1026	5.65	1047	1.82	21
1401	2.45	1402	1.66	1
1465	4.34	1465	4.16	0
2073	3.77	2318	2.27	245
2870	14.6	2854	5.26	-16
2925	8.11	2923	9.05	-2
2941	9.28	2954	4.54	13

Note: The anion's predicted P-H stretch is shaded.

The calculations do a very good job for predicting most of the band frequencies with the exception of the P-H stretch. The calculations tend to overestimate the relative intensities for higher frequencies and underestimate for lower frequencies. The anion's P-H stretch is very broad, and is also shifted several orders of magnitude from the calculated position.

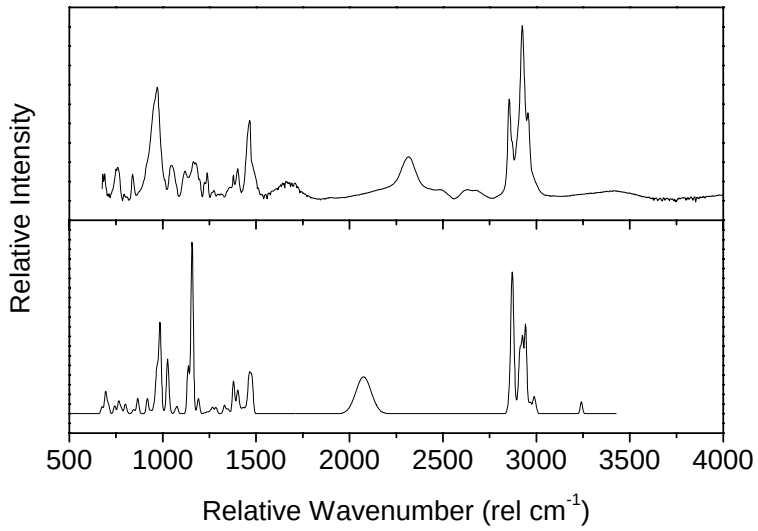

Figure 3.15: The experimental infrared spectrum (Top) and the predicted infrared spectrum (Bottom) for the ionic liquid $[Et_3NH]^+[(octyl)PO_2H]^-$.

Table 3.9: Major infrared intensities (predicted intensities greater than 10) for the ionic liquid $[Bu_4N]^+[(hexyl)PO_2H]^-$.

Cation B3LYP 6-31G(d)		Anion B3LYP 6-31G(d)	
Frequency	Infrared Intensity	Frequency	Infrared Intensity
783.318	10.389	381.457	23.268
870.869	23.337	455.146	13.776
904.252	12.384	486.857	23.291
918.239	16.683	711.460	22.804
1049.152	11.840	735.292	20.675
1061.953	10.438	742.918	12.981
1396.256	18.457	780.961	20.183
1529.985	10.601	858.158	18.077
1537.481	18.162	947.669	35.594
1545.924	13.211	1003.005	10.954
3035.722	15.456	1048.956	37.621
3038.983	12.248	1058.691	25.186
3044.831	11.757	1061.765	25.364
3048.736	26.335	1103.033	136.577
3050.554	21.176	1134.780	27.822
3054.686	18.230	1216.329	28.559
3055.296	15.456	1273.626	137.745
3061.381	21.278	1280.334	36.036
3065.357	10.215	1291.349	94.588
3070.328	17.500	2152.041	446.805
3072.673	25.101	3010.586	58.544
3094.482	14.288	3019.372	50.138
3122.556	37.587	3079.858	80.309
3129.726	17.594	3093.954	63.635
3131.854	11.042	3098.622	83.820
3132.777	31.778		
3132.904	21.458		
3157.551	21.387		
3166.834	21.508		

Note: The anion's predicted P-H stretch is shaded. No other bands on the cation or anion are predicted near 2000 rel cm^{-1}.

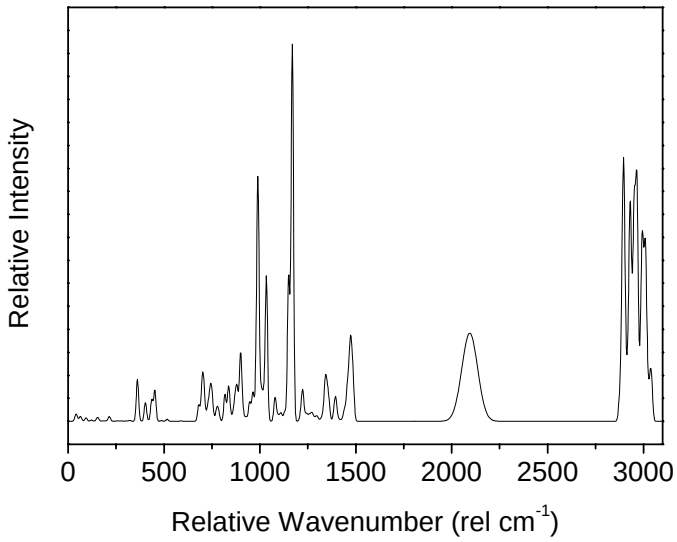

Figure 3.16: The calculated infrared spectrum of the ionic liquid $[Bu_4N]^+[(hexyl)PO_2H]^-$.

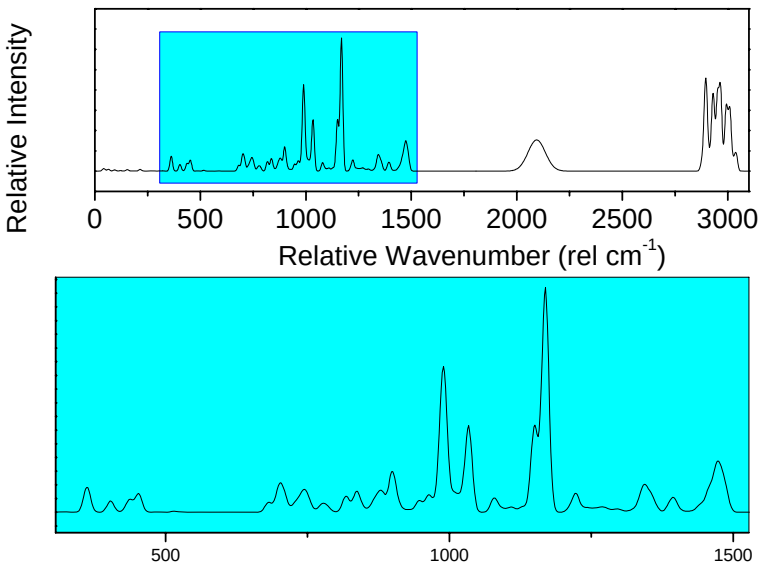

Figure 3.17: A zoom plot of the predicted infrared spectrum for the ionic liquid $[Bu_4N]^+[(hexyl)PO_2H]^-$.

The predicted spectrum's frequency was multiplied by 0.9540 to allow better agreement with experimental frequencies [16]. A comparison between the predicted and experimental frequencies is given by Table 3.10 and Figure 3.18.

Table 3.10: Comparison between predicted and experimental frequencies.

Predicted Band		Experimental Band		Difference in
Frequency	Relative Intensity	Frequency	Relative Intensity	Frequency Δf
898	2.97	883	4.92	-15
989	10.64	941	0.937	-48
1032	6.1	1041	10.2	9
1169	16.4	1176	9.58	7
1395	1.06	1380	2.86	-15
1469	3.47	1488	4.53	19
2095	3.83	2246	1.389	151
2896	11.47	2873	5.46	-23
2931	9.57	2933	7.38	2
2964	10.9	2960	8.51	-4

Note: The anion's predicted P-H stretch is shaded.

The calculations do a good job for predicting most of the band frequencies with the exception of the P-H stretch. The calculations tend to underestimate the relative intensities. The anions P-H stretch is very broad and is also shifted several orders of magnitude from the calculated position. In the experimental infrared spectrum there is a broad band at 3300 rel cm^{-1} which is due to the presence of a small amount of H_2O in the sample.

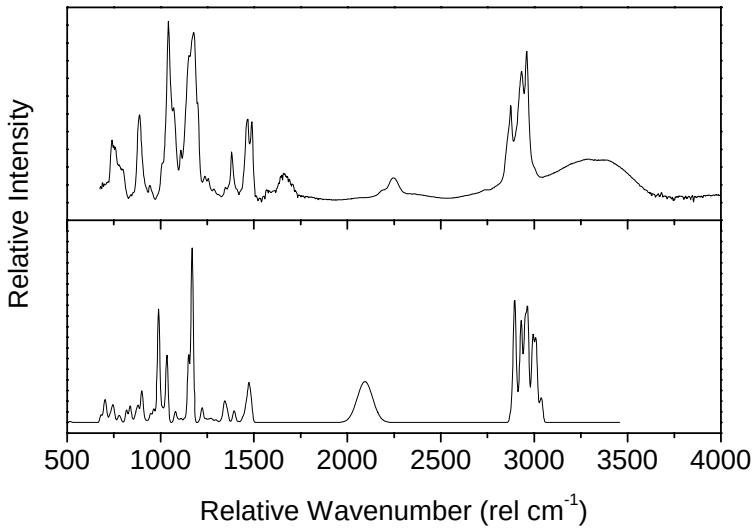

Figure 3.18: The experimental infrared spectrum and the bottom spectrum (Top) shows the predicted infrared spectrum (Bottom) for the ionic liquid $[Bu_4N]^+[hexylPO_2H]^-$.

Table 3.11: Major infrared intensities (predicted intensities greater than 10) for the ionic liquid $[Bu_4P]^+[(octyl)_2PO_2]^-$.

Cation		Anion	
B3LYP 6-31G(d)		B3LYP 6-31G+(dp)	
Frequency	Infrared Intensity	Frequency	Infrared Intensity
747.835	14.437	421.766	25.672
807.527	13.653	462.523	27.132
819.245	15.684	476.595	33.849
929.392	13.163	760.030	83.715
941.170	24.376	785.865	49.253
1007.463	10.990	845.563	16.019
1111.975	12.241	1003.770	13.809
1121.005	48.506	1012.572	12.893
1124.925	21.052	1026.454	158.133
1127.478	11.731	1067.684	16.242
1488.000	19.171	1186.475	102.615
1530.399	11.041	1204.619	13.591
1530.944	10.219	1210.494	111.965
1538.068	13.373	1212.024	58.282
3036.929	11.376	1251.213	18.397
3043.619	53.698	1254.418	13.334
3053.846	5.665	1459.193	16.973
3054.054	24.384	1516.151	16.388
3054.446	17.498	2992.597	14.861
3054.683	27.662	3007.518	61.487
3085.234	19.801	3023.865	31.840
3087.041	11.706	3046.509	11.718
3105.284	15.077	3053.102	23.599
3119.439	82.020	3053.123	11.021
3119.968	48.479	3060.109	52.693
3120.734	51.671	3060.382	111.785
3134.525	26.748	3076.114	102.336
3134.635	13.164	3089.836	120.372
3134.741	18.900	3091.005	41.111
		3091.034	116.422

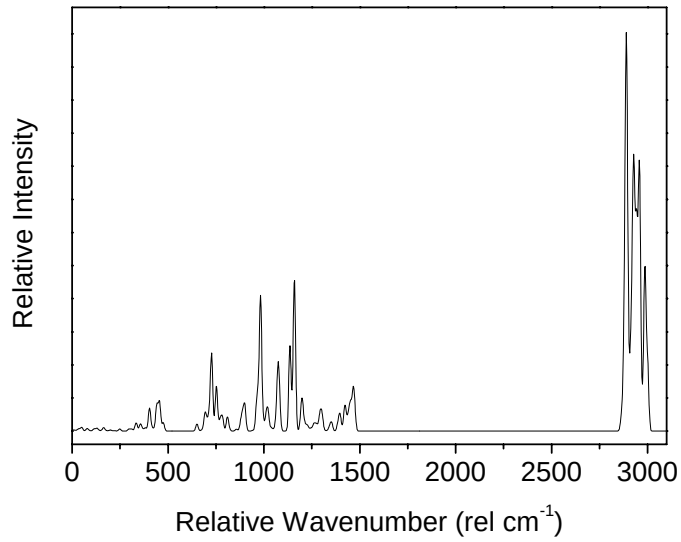

Figure 3.19: The calculated infrared spectrum of the ionic liquid $[Bu_4P]^+[(octyl)_2PO_2]^-$.

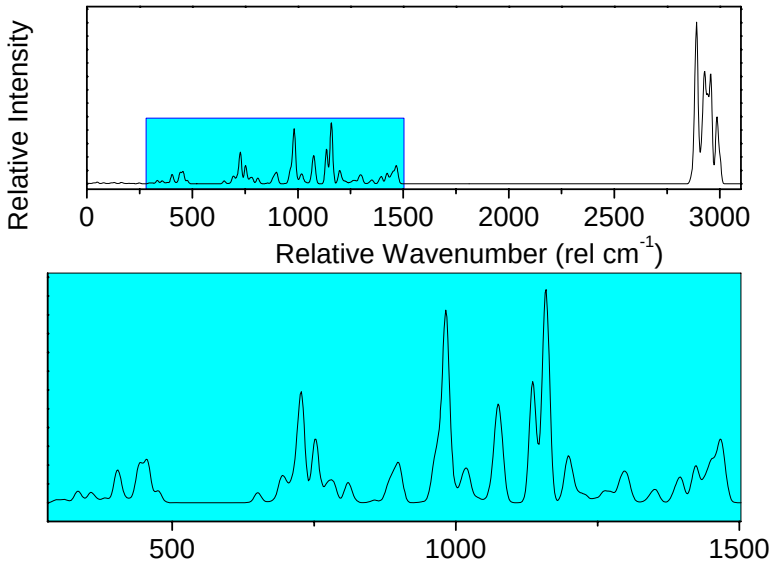

Figure 3.20: A zoom plot of the predicted infrared spectrum for the ionic liquid $[Bu_4P]^+[(octyl)_2PO_2]^-$.

The predicted spectrum's frequency was multiplied by 0.9726 to allow better agreement with experimental frequencies [16]. A comparison between the predicted and experimental frequencies is given by Table 3.12 and Figure 3.21.

Table 3.12: Comparison between predicted and experimental frequencies.

Predicted Band		Experimental Band		Difference in
Frequency	Relative Intensity	Frequency	Relative Intensity	Frequency Δf
899	2.1	919	2.81	20
1074	5.24	1097	2.91	23
1159	11.35	1168	12.59	9
1198	2.49	1214	1.75	16
1395	1.36	1378	2.12	-17
1423	1.96	1409	1.75	-14
1466	3.39	1463	5.29	-3
2889	30.1	2856	6.53	-33
2957	20.46	2925	12.16	-32
2987	12.45	2958	7.8	-29

The calculations do a very good job for predicting most of the band frequencies. The calculations do a good job of estimating the relative intensities at lower frequencies but overestimate relative intensities at higher frequencies. This ionic liquid does not have a P-H group so the 1500-2750 rel cm^{-1} region is empty.

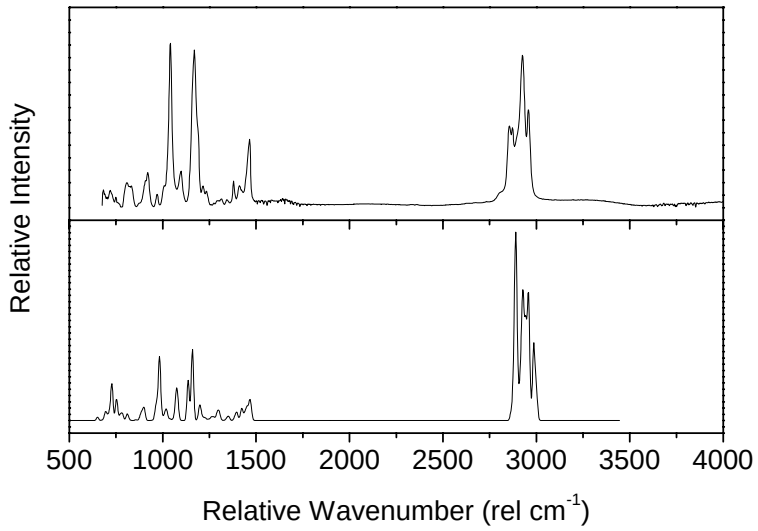

Figure 3.21: The experimental infrared spectrum (Top) and the predicted infrared spectrum (Bottom) for the ionic liquid $[Bu_4P]^+[(octyl)_2PO_2]^-$.

3.5 Discussion of Gaussian Calculations

The experimental Raman and infrared peaks look broad and intertwined. Closer inspection of the predicted spectra shows that the broadening is due to the close proximity of numerous bands, see Figure 3.22. Hence, the scattering cross sections of the ionic liquids were found for groups of bands rather than individual bands.

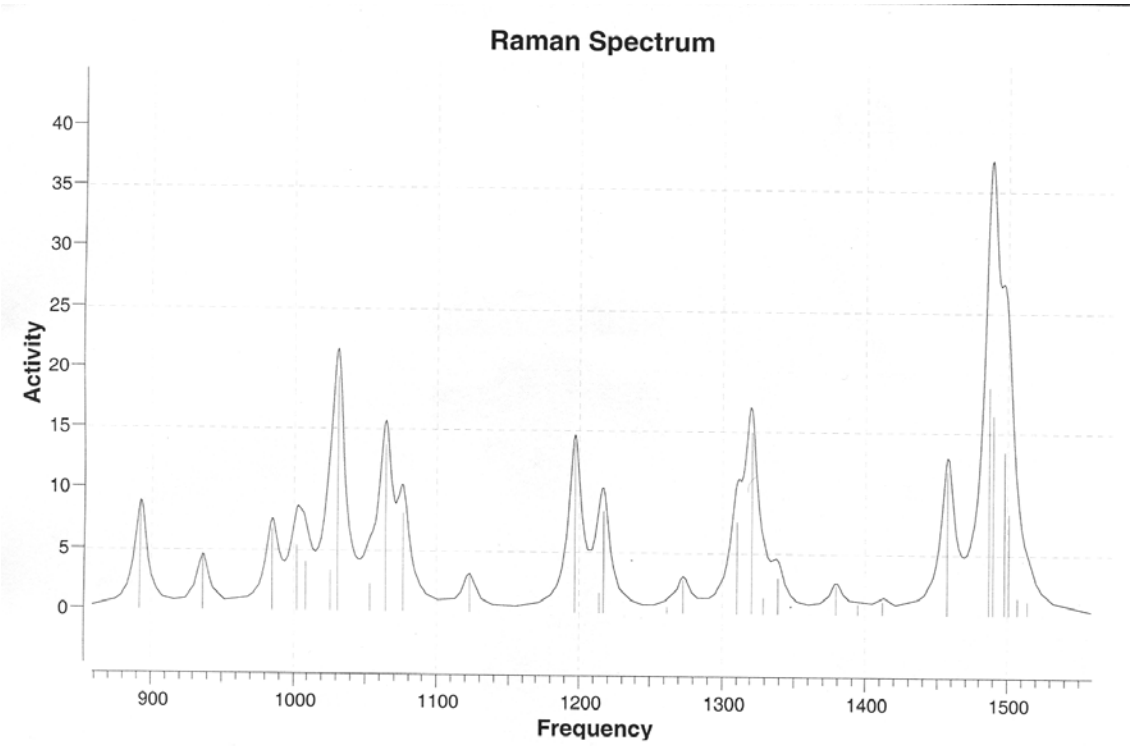

Figure 3.22: The predicted spectrum of the anion PO_2H(hexyl) illustrating that numerous bands are involved in forming peaks.

Overall the predicted spectra were close to the experimental spectra obtained implying that no underlying anomalous effects were perturbing the spectra. However, the calculations poorly estimated the position of the P-H of the ionic liquids. This could be due to the anions forming dimer pairs with each other or that the P-H mode was on the charged end of the anion. By adding diffuse functions to the hydrogen atoms (i.e. using ++ with the calculations, see section 3.1) perhaps better agreement with experimental results could be obtained. Previous DFT studies on tetra-alkyl phosphonium cations predicted the P-H stretch to be at 2298 cm^{-1} [17], which is close to the Raman and infrared experimental values that ranged from 2246-2325cm^{-1}.

Chapter Four

Raman and Infrared Band Assignments

4.0 Introduction to Raman and Infrared Band Assignments

In this section the major peaks of the ionic liquids Raman and infrared spectra are assigned [18, 19]. The assigned vibrational modes may be viewed if reader has access to Gauss View 3.0, by simply opening the output LOG file located on the appended DVD with Gauss View 3.0 and clicking on the vibrational results menu. In Chapter 3 the frequency was shifted by a scaling factor, the unshifted frequencies have been tabulated in addition to the shifted frequencies to allow the modes to be located in Gauss view 3.0. The ionic liquid peaks fitted to determine the differential scattering cross section in Chapter Five correspond to groups of bands rather than a single band and so can not be assigned a single mode.

4.1 Raman Band Assignments

Table 4.1: Raman band assignments for the ionic liquid $[Et_3NH]^+[(octyl)PO_2H]^-$.

Unshifted	Predicted	Experimental	Assignments
708	699	763	anion CH bend in plane CH rocking on C_1, C_2, C_3
1083	1080	1059	cation asymmetrical C-C-N stretching N-H wag, CH out of plane twisting
1317	1299	1304	anion CH out of plane twisting
1447	1425	1406	cation asymmetrical C-C-N stretching N-H wag, CH out of plane twisting
1491	1456	1455	anion symmetrical C-C-C stretching symmetrical CH stretching
2179	2086	2325 broad	anion P-H stretching
3073	2922	2949	anion symmetrical CH stretching on C_7 asymmetrical CH stretching on C_8
3103	2999	3035	cation asymmetrical CH stretching on C1, C2

Calculation level: B3LYP 6-311G on $[Et_3NH]^+$ and B3LYP 6-31+G(d, p) on $[(octyl)PO_2H]^-$.

Table 4.2: Raman band assignments for the ionic liquid $[Bu_4N]^+[hexylPO_2H]^-$.

Unshifted	Predicted	Experimental	Assignments
1002	982	903	anion symmetrical C-C-C stretching on C_5 PH wag, CH out of plane twisting
1034	1015	1050	anion symmetrical PO stretching PH wag, C-C-C asymmetrical stretching
1360	1332	1323	cation CH out of plane twisting
1457	1420	1409	anion scissoring on C_1, C_2
2179	2079	2252	anion PH stretching
2999	2947	2969	anion CH symmetrical stretching
3019	3019	3010	cation CH symmetrical stretching

Calculation level: B3LYP 6-31G(d) on $[Bu_4N]^+$and B3LYP 6-31+G(d,p) on $[(hexyl)PO_2H]^-$.

Table 4.3: Raman band assignments for the ionic liquid $[Bu_4P]^+[(octyl)_2PO_2]^-$.

Unshifted	Predicted	Experimental	Assignments
686	662	680	anion C-P-C symmetrical stretching C-C-C symmetrical stretching
905	887	888	cation C-C-C symmetrical stretching CH_2 in plane rocking
1358	1320	1300	cation CH_2 out of plane twisting
1480	1448	1410	anion CH_2 scissoring on C_1, C_2, C_3, C_4
1507	1478	1450	anion CH_2 scissoring
3001	2935	2924	anion CH_2 symmetrical stretching
3036	2985	3004	cation CH_2 symmetrical stretching

Calculation level: B3LYP 6-31G(d) on $[Bu_4P]^+$and B3LYP 6-31+G(d) on $[(octyl)_2PO_2]^-$.

4.1 Infrared Band Assignments

Table 4.4: Infrared band assignments for the ionic liquid $[Et_3NH]^+[(octyl)PO_2H]^-$.

Unshifted	Predicted	Experimental	Assignments
802	765	759	cation C-N-N asymmetrical stretching CH_2 in plane rocking
1034	1026	1047	anion C-C-C symmetrical stretching on C_4 CH_2 out of plane twisting, P-H wag
1447	1401	1402	cation C-N-C asymmetric stretching N-H wag, CH_2 in plane rocking
2179	2073	2318	anion P-H stretching
3009	2870	2854	anion CH_2 symmetric stretching
3015	2941	2954	cation CH_2 asymmetric stretching

Calculation level: B3LYP 6-311G on $[Et_3NH]^+$ and B3LYP 6-31+G(d,p) on $[(octyl)PO_2H]^-$

Table 4.5: Infrared band assignments for the ionic liquid $[Bu_4N]^+[hexylPO_2H]^-$.

Unshifted	Predicted	Experimental	Assignments
918	898	883	cation C-N-C symmetric stretching CH_2 in plane rocking
1076	1032	1041	anion O-C-C symmetric stretching P-H wag, CH_2 out of plane wag
1451	1395	1380	cation CH_3 umbrella mode CH_2 out of plane wagging
1529	1469	148	cation CH_2 in plane scissoring CH_3 in plane scissoring
2179	2095	2246	anion P-H wag
3011	2896	2973	anion CH_2 symmetric stretching on C_1, C_4, C_5 CH_2 asymmetric stretching on C_2, C_3
3088	2964	2960	anion CH_2 asymmetric stretching CH_3 asymmetric stretching

Calculation level: B3LYP 6-31G(d) on $[Bu_4N]^+$and B3LYP 6-31+G(d,p) on $[(hexyl)PO_2H]^-$.

Table 4.6: Infrared assignments for the ionic liquid $[Bu_4P]^+[(octyl)_2PO_2]^-$.

Unshifted	Predicted	Experimental	Assignments
929	899	919	cation CH_2 out of plane twisting
1193	1159	1168	anion CH_2 out of plane wagging O-P-O asymmetric stretching
1488	1423	1409	cation CH_2 in plane scissoring
1520	1466	1463	anion CH_3 in plane scissoring
2992	2889	2856	anion CH2 symmetric stretching
3043	2987	2958	cation CH_2 symmetric stretching

Calculation level: B3LYP 6-31G(d) on $[Bu_4P]^+$and B3LYP 6-31+G(d) on $[(octyl)_2PO_2]^-$.

Chapter Five
A-Term Fitting to Raman Data

5.0 Introduction to A-term Fitting to Raman Data

The data corrections and processes outlined in Chapter One are developed further in this chapter, and applied to obtain graphs for A-term fitting. Graphs of differential cross section versus excitation energy were prepared and fitted to extract the parameters dimensionless coupling constant, K_{diff}, and effective excited state frequency, ν_e. These numbers allow the scattering cross section of the ionic liquids band to be calculated for any wavelength. The absolute scattering cross section of the ionic liquids were also calculated for the bands investigated.

5.1 Data processing for A-term graphs

The A-term graphs required for the determination of K and ν_e are simply plots of the differential scattering cross section versus excitation energy for each band. Before the band areas can be integrated to determine the differential scattering cross section, the background must be subtracted off and a correction must be made to account for the collection efficiency of the optics used. This can be achieved using the equation given in Chapter One:

$$I_{corrected} = \lambda^2 \left(\frac{I_{known}}{I_{experimental}} \right) I_{uncorrected}$$

After the intensity corrections are applied the areas of the chosen bands of the ionic liquid may then be integrated as shown in Figure 5.1. As only the total area of the band is needed for the integration the peak may be evaluated with numerous curves to get a very good fit. In addition to the ionic liquid bands being integrated a set of standard bands were integrated with a known differential cross section. The standards used in this thesis are cyclohexane, carbon tetrachloride, benzene and dichloromethane. Acetonitrile was used instead of benzene for the 416 nm wavelength as the 992 cm^{-1} mode of benzene was found to saturate the A/D converter of the

detector after a few seconds of collection. This saturation was due to resonance effects.

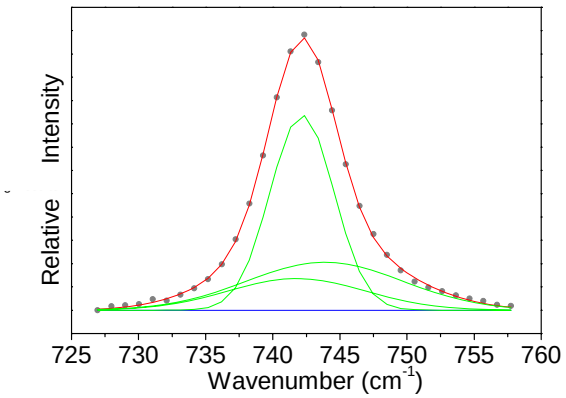

Figure 5.1: The 742 cm^{-1} mode of $[CH_3N(C_4H_8)Bu]^+[(F_3CSO_2)_2N]^-$ fitted with three gaussian curves using the peak fitting module of Origin 7.5. Gaussian curves were fitted to broad peaks and Lorentzian curves to sharp peaks.

Table 5.1: The Differential scattering cross sections of known standards from literature [20-22].

Excitation Wavelength (nm)	Cyclohexane 801 cm^{-1}	Carbon tetrachloride 775 cm^{-1}	Benzene 992 cm^{-1}	Dichloromethane 701 cm^{-1}	Acetonitrile 918 cm^{-1}
416	22.87	33	95.17	27.85	2.95
487	11.07	12	42.29	15.05	1.54
514	8.67	8	32.33	12.19	1.23
532	7.42	7	27.30	10.66	1.07
633	3.41	3	11.82	5.43	0.52

Note: All differential cross sections are in units of μb sr^{-1}

To determine the differential scattering cross section the equation derived in Chapter One was used:

$$\left(\frac{\partial\sigma_R}{\partial\Omega}\right)_1 = \frac{I_1}{I_2}\left(\frac{n_1}{n_2}\right)^2 \frac{\rho_2}{\rho_1}\left(\frac{\partial\sigma_R}{\partial\Omega}\right)_2$$

As the refractive index, density and differential cross section are all constant for the wavelength being investigated, only the ratio of the area of the ionic liquid and solvent band was needed for the determination of the differential scattering cross section of the ionic liquid band. The refractive index was found using a refractometer at 20ºC and the density by placing one mL of ionic liquid into a volumetric flask and weighing it.

Table 5.2: Refractive index and density of the ionic liquids.

	$[CH_3N(C_4H_8)Bu]^+$ $[(F_3CSO_2)_2N]^-$	**$[Et_3NH]^+$ $[(octyl)PO_2H]^-$**	**$[Bu_4N]^+$ $[(hexyl)PO_2H]^-$**	**$[Bu_4P]^+$ $[(octyl)_2PO_2]^-$**
Refractive index	1.420	1.460	1.460	1.470
Density ρ (mol dm^{-3})	3.33	3.78	2.37	1.40

5.2 A-term Fitting to Ionic Liquid Raman Data

Using the previous equation for the differential scattering cross section and the ratios of the peak areas, the scattering differential cross section was obtained using the different standards at five different wavelengths. Unfortunately, the dichloromethane 701 cm^{-1} doublet for the 416 nm data did not completely fit on the window collected and could not be used as a standard. For simplicity only the final values of the differential scattering cross section is presented. A complete set of the calculations, spectra and fitted peak areas can be found on the appended DVD. The equation given in Chapter One section 1.6 was modified to allow A-terms to be fitted to differential instead of absolute scattering cross sections:

$$\left(\sigma_R\right)_{m,n} = KF_A\left(\nu_0\right)^2$$

$$\frac{8\pi}{3}\left(\frac{1+2\rho}{1+\rho}\right)\frac{\partial\sigma_R}{\partial\Omega} = KF_A\left(\nu_0\right)^2$$

$$\frac{\partial\sigma_R}{\partial\Omega} = \frac{3}{8\pi}\left(\frac{1+\rho}{1+2\rho}\right)KF_A\left(\nu_0\right)^2$$

$$\boxed{\frac{\partial\sigma_R}{\partial\Omega} = K_{diff}\left(\nu_0-\nu_{vib}\right)^2\left(\frac{\nu_e^2+\nu_0^2}{\left(\nu_e^2-\nu_0^2\right)^2}\right)^2}$$

Where

$$K_{diff} = \frac{3}{8\pi}\left(\frac{1+\rho}{1+2\rho}\right)K$$

$$\nu = \nu_0 - \nu_{vib}$$

Where ν_{vib} is the vibrational frequency of the band being investigated, K_{diff} is the differential coupling constant and all other terms have been defined previously. To calculate the absolute scattering cross sections and the coupling constants the depolarization ratios of the bands are required. The depolarization ratios were obtained by the method outlined in Chapter Two. Origin 7.5 non-linear peak fitting module was used to fit the equation and determine the parameters K_{diff} and ν_e. The fitted data and all spreadsheets may be found on the appended DVD.

Table 5.3: The depolarization ratios of the ionic liquid bands.

Chemical Species	Raman Shift (cm^{-1})	Depolarization Ratio
$[CH_3N(C_4H_8)Bu]^+[(F_3CSO_2)_2N]^-$	741	0.20
	1240	0.47
$[Et_3NH]^+[(octyl)PO_2H]^-$	1300	0.59
	1452	0.55
$[Bu_4N]^+[(hexyl)PO_2H]^-$	1477	0.57
$[Bu_4P]^+[(octyl)_2PO_2]^-$	1298	0.88
	1447	0.71

Error bars to define the 95% confidence interval were added to the differential cross section in the A-term plots by using the equation:

$$Error = \frac{\sigma_{n-1}}{\sqrt{n}} t$$

Where σ_{n-1} is the standard deviation, n is the number of samples and t is the appropriate factor from the t-table. This method does not take into account any systematic errors that would have occurred.

Table 5.4: The differential scattering cross sections of the 742 cm^{-1} band of $[CH_3N(C_4H_8)Bu]^+[(F_3CSO_2)_2N]^-$.

Excitation Wavelength (nm)	Relative to Cyc μb sr^{-1}	Relative to Ctet μb sr^{-1}	Relative to Benz μb sr^{-1}	Relative to Dcm μb sr^{-1}	Relative to Aceto μb sr^{-1}	Average μb sr^{-1}	Std Dev μb sr^{-1}
416	34.63	34.06			25.74	31.47	4.98
487	19.87	17.70	14.41	17.85		17.46	2.26
514	16.78	14.66	13.28	15.57		15.07	1.48
532	14.00	11.12	11.53	12.60		12.31	1.29
633	5.47	4.39	4.83	6.56		5.31	0.94

Table 5.5: The absolute scattering cross sections of the 742 cm^{-1} band of $[CH_3N(C_4H_8)Bu]^+[(F_3CSO_2)_2N]^-$.

Excitation Wavelength (nm)	Relative to Cyc μb	Relative to Ctet μb	Relative to Benz μb	Relative to Dcm μb	Relative to Aceto μb	Average μb	Std Dev μb
416	337	332			251	307	48
487	194	172	140	174		170	22
514	164	143	129	152		147	14
532	136	108	112	123		120	13
633	53	43	47	64		52	9

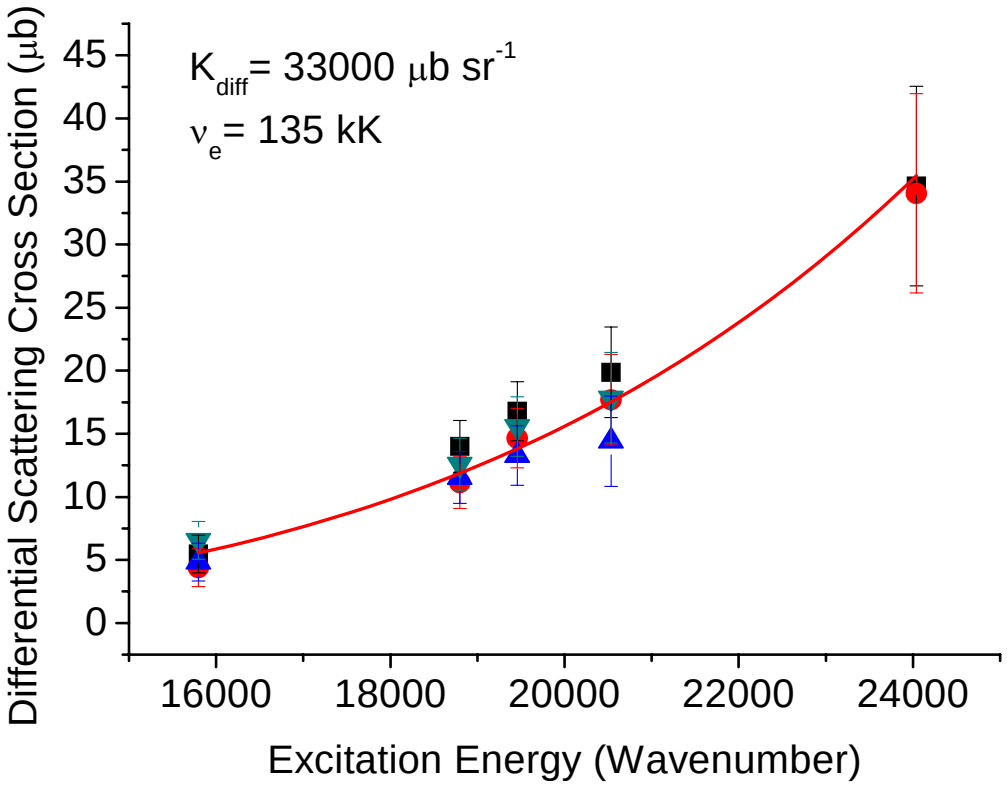

Figure 5.2: Plot of differential scattering cross section vs. excitation energy for the 742 cm^{-1} band of $[CH_3N(C_4H_8)Bu]^+[(F_3CSO_2)_2N]^-$ with an A-term equation fitted to extract parameters K_{diff} and ν_e.

Table 5.6: The differential scattering cross sections of the 1241 cm^{-1} band of $[CH_3N(C_4H_8)Bu]^+[(F_3CSO_2)_2N]^-$.

Excitation Wavelength (nm)	Relative to Cyc μb sr^{-1}	Relative to Ctet μb sr^{-1}	Relative to Benz μb sr^{-1}	Relative to Dcm μb sr^{-1}	Relative to Aceto μb sr^{-1}	Average μb sr^{-1}	Std Dev μb sr^{-1}
416	22.16	21.69			20.68	21.51	0.76
487	6.95	6.16	5.99	6.18		6.32	0.43
514	7.88	6.81	7.70	7.32		7.43	0.48
532	7.67	4.87	5.93	5.52		6.00	1.20
633	3.00	2.41	2.92	3.59		2.98	0.49

Table 5.7: The absolute scattering cross sections of the 1241 cm^{-1} band of $[CH_3N(C_4H_8)Bu]^+[(F_3CSO_2)_2N]^-$.

Excitation Wavelength (nm)	Relative to Cyc μb	Relative to Ctet μb	Relative to Benz μb	Relative to Dcm μb	Relative to Aceto μb	Average μb	Std Dev μb
416	245	240			228	238	8
487	77	68	66	68		70	5
514	87	75	85	81		82	5
532	85	54	66	61		66	13
633	33	27	32	40		33	5

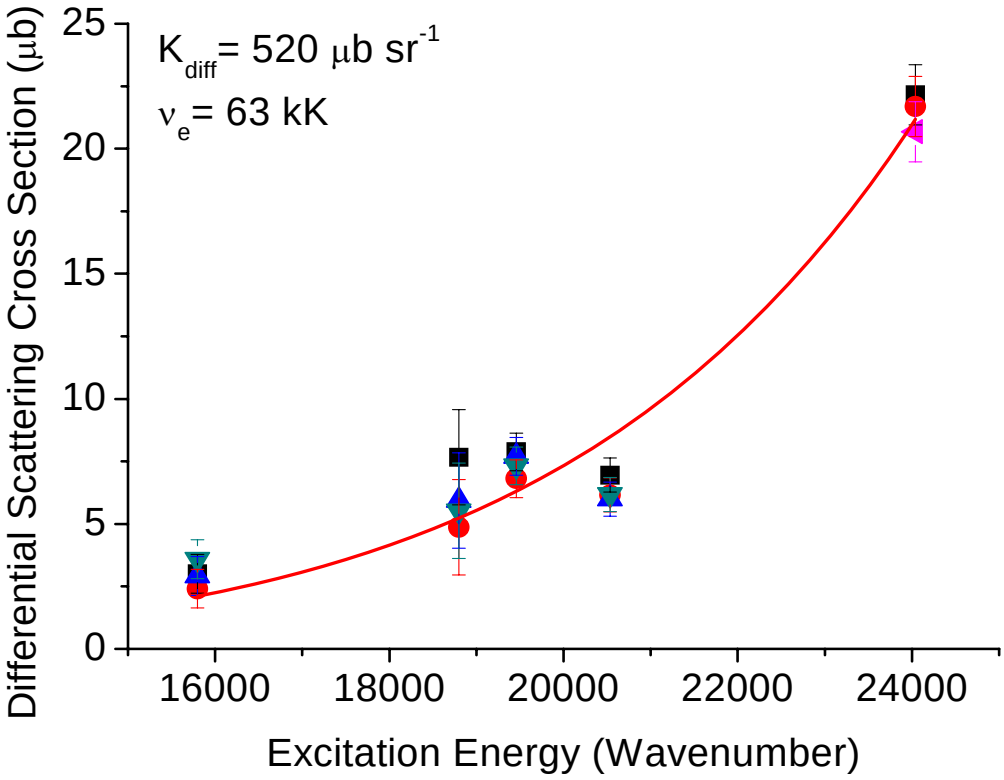

Figure 5.3: Plot of differential scattering cross section vs. excitation energy for the 1241 cm^{-1} band of $[CH_3N(C_4H_8)Bu]^+[(F_3CSO_2)_2N]^-$.

Table 5.8: The differential scattering cross sections of the 1300 cm^{-1} band of $[Et_3NH]^+[(octyl)PO_2H]^-$.

Excitation Wavelength (nm)	Relative to Cyc μb sr^{-1}	Relative to Ctet μb sr^{-1}	Relative to Benz μb sr^{-1}	Relative to Dcm μb sr^{-1}	Relative to Aceto μb sr^{-1}	Average μb sr^{-1}	Std Dev μb sr^{-1}
416	15.38	16.05			13.72	15.05	15.38
487	4.11	3.68	3.09	3.19		3.52	4.11
514	5.79	5.06	5.27	5.39		5.38	5.79
532	4.69	3.73	4.44	4.23		4.27	4.69
633	1.55	1.24	1.51	1.99		1.57	1.55

Table 5.9: The absolute scattering cross sections of the 1300 cm^{-1} band of $[Et_3NH]^+[(octyl)PO_2H]^-$.

Excitation Wavelength (nm)	Relative to Cyc μb	Relative to Ctet μb	Relative to Benz μb	Relative to Dcm μb	Relative to Aceto μb	Average μb	Std Dev μb
416	177	184			158	173	14
487	47	42	36	37		40	5
514	67	58	61	62		62	4
532	54	43	51	49		49	5
633	18	14	17	23		18	4

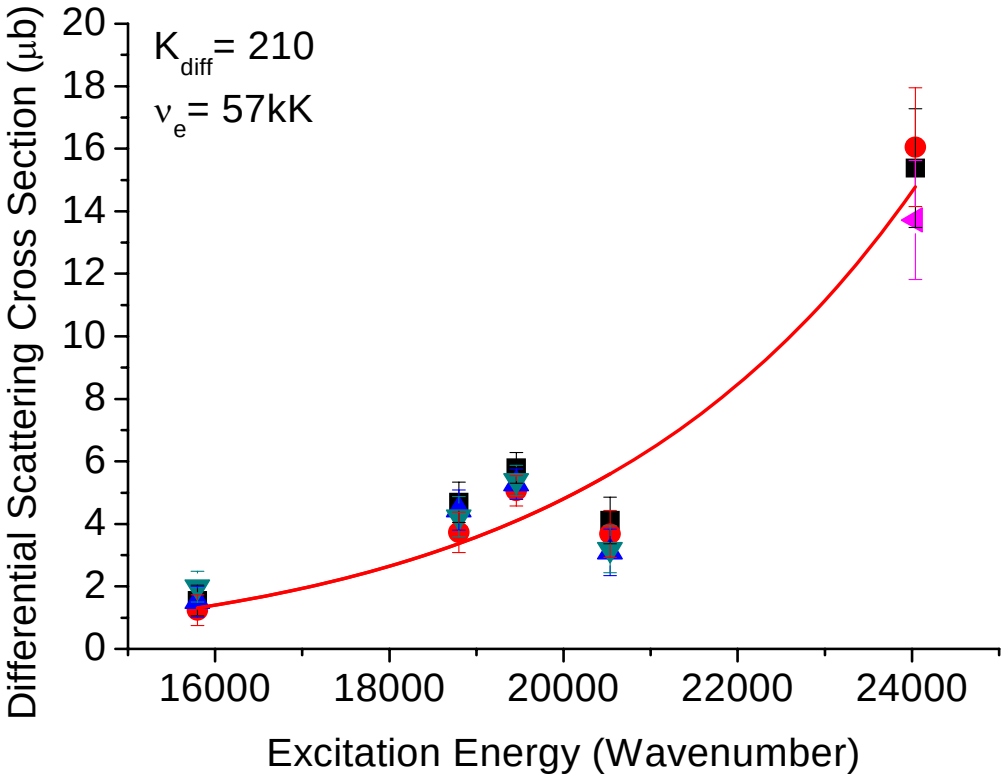

Figure 5.4: Plot of differential scattering cross section vs. excitation energy for the 1300 cm^{-1} band of $[Et_3NH]^+[(octyl)PO_2H]^-$.

Table 5.10: The differential scattering cross sections of the 1452 cm^{-1} band of $[Et_3NH]^+[(octyl)PO_2H]^-$.

Excitation Wavelength (nm)	Relative to Cyc μb sr^{-1}	Relative to Ctet μb sr^{-1}	Relative to Benz μb sr^{-1}	Relative to Dcm μb sr^{-1}	Relative to Aceto μb sr^{-1}	Average μb sr^{-1}	Std Dev μb sr^{-1}
416	47.16	45.83			43.84	45.61	1.68
487	13.73	12.25	11.96	12.39		12.58	0.79
514	21.62	17.70	19.69	20.07		19.77	1.61
532	14.54	11.58	13.81	13.12		13.26	1.26
633	6.22	5.04	5.50	6.77		5.88	0.77

Table 5.11: The absolute scattering cross sections of the 1452 cm^{-1} band of $[Et_3NH]^+[(octyl)PO_2H]^-$.

Excitation Wavelength (nm)	Relative to Cyc μb	Relative to Ctet μb	Relative to Benz μb	Relative to Dcm μb	Relative to Aceto μb	Average μb	Std Dev μb
416	535	520			497	517	19
487	156	139	136	140		143	9
514	245	201	223	228		224	18
532	165	131	157	149		150	14
633	71	57	62	77		67	9

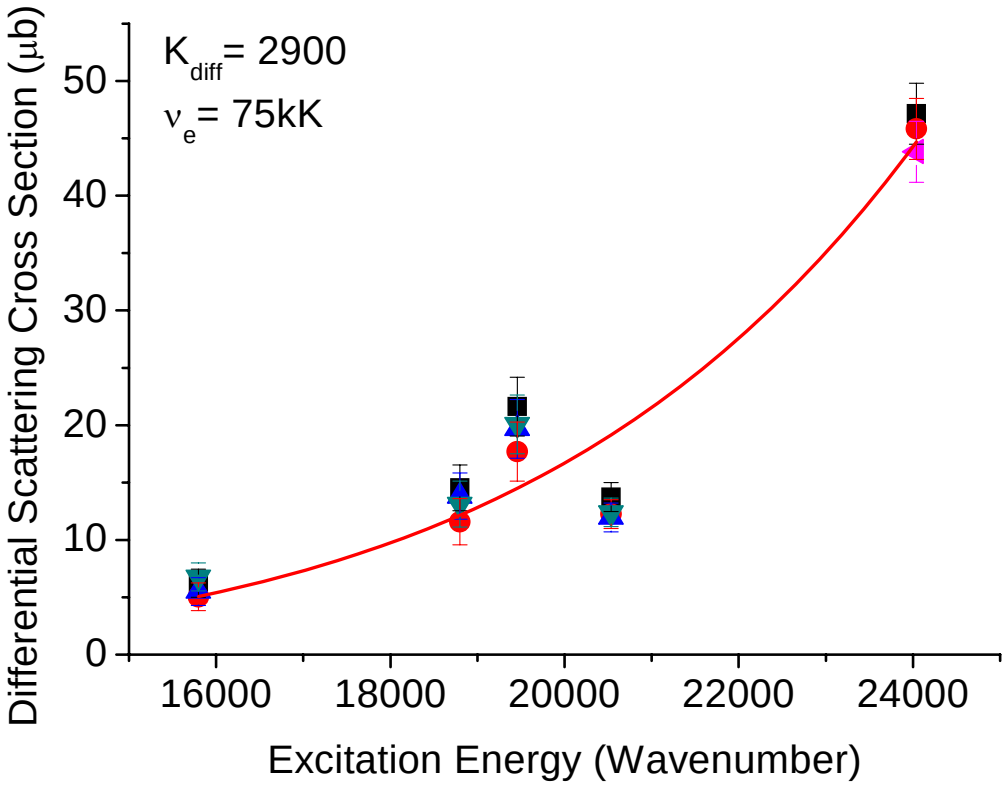

Figure 5.5: Plot of differential scattering cross section vs. excitation energy for the 1452 cm^{-1} band of $[Et_3NH]^+[(octyl)PO_2H]^-$.

Table 5.12: The differential scattering cross sections of the 1447 cm^{-1} band of $[Bu_4N]^+[(hexyl)PO_2H]^-$.

Excitation Wavelength (nm)	Relative to Cyc μb sr^{-1}	Relative to Ctet μb sr^{-1}	Relative to Benz μb sr^{-1}	Relative to Dcm μb sr^{-1}	Relative to Aceto μb sr^{-1}	Average μb sr^{-1}	Std Dev μb sr^{-1}
416	80.13	77.82			74.66	77.54	2.75
487	30.11	28.79	28.12	28.96		29.00	0.82
514	39.00	34.29	35.64	36.73		36.42	1.99
532	28.94	22.97	18.53	26.20		24.16	4.48
633	0.46	0.37	0.45	0.56		0.46	0.08

Table 5.13: The absolute scattering cross sections of the 1447 cm^{-1} band of $[Bu_4N]^+[(hexyl)PO_2H]^-$.

Excitation Wavelength (nm)	Relative to Cyc μb	Relative to Ctet μb	Relative to Benz μb	Relative to Dcm μb	Relative to Aceto μb	Average μb	Std Dev μb
416	913	887			851	884	31
487	343	328	321	330		331	9
514	445	391	406	419		415	23
532	330	262	211	299		275	51
633	5	4	5	6		5	1

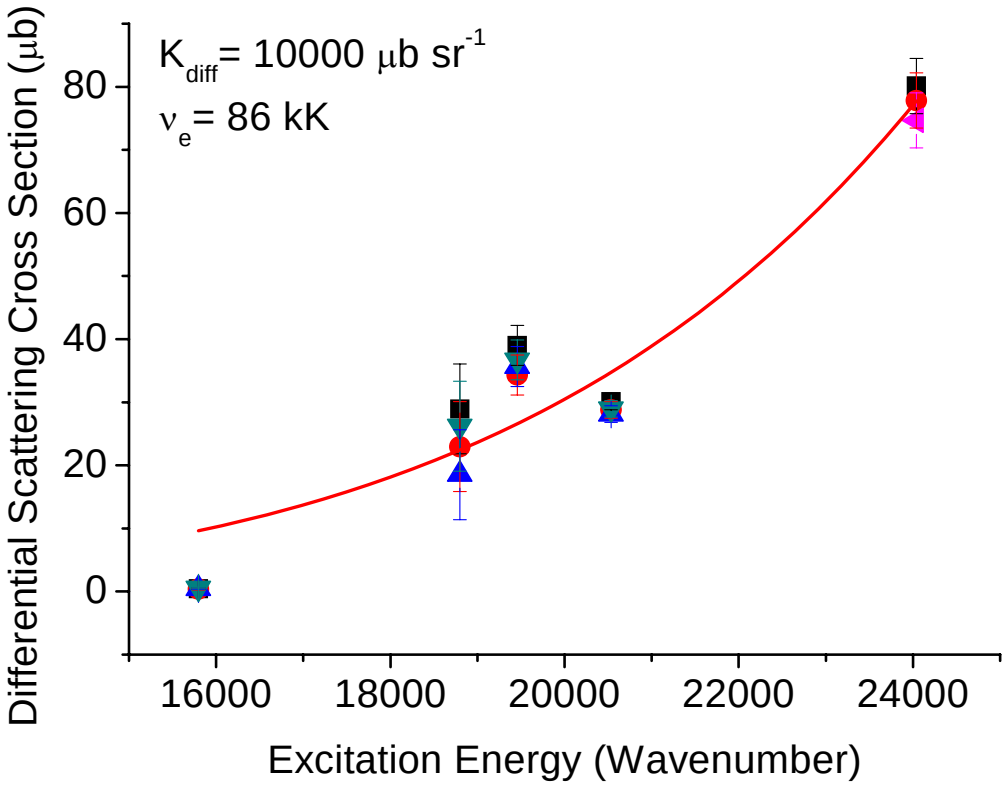

Figure 5.6: Plot of differential scattering cross section vs. excitation energy for the 1447 cm^{-1} band of $[Bu_4N]^+[(hexyl)PO_2H]^-$.

Table 5.14: The differential scattering cross sections of the 1298 cm^{-1} band of $[Bu_4P]^+[(octyl)_2PO_2]^-$.

Excitation Wavelength (nm)	Relative to Cyc μb sr^{-1}	Relative to Ctet μb sr^{-1}	Relative to Benz μb sr^{-1}	Relative to Dcm μb sr^{-1}	Relative to Aceto μb sr^{-1}	Average μb sr^{-1}	Std Dev μb sr^{-1}
416	52.32	50.06			45.48	49.29	3.49
487	48.92	47.36	46.18	47.45		47.48	1.12
514	19.01	16.58	17.29	17.67		0.00	1.02
532	13.48	10.71	19.88	12.22		14.07	4.03
633	0.48	0.40	0.25	0.31		0.36	0.10

Table 5.15: The absolute scattering cross sections of the 1298 cm^{-1} band of $[Bu_4P]^+[(octyl)_2PO_2]^-$.

Excitation Wavelength (nm)	Relative to Cyc μb	Relative to Ctet μb	Relative to Benz μb	Relative to Dcm μb	Relative to Aceto μb	Average μb	Std Dev μb
416	643	616			559	606	43
487	602	582	568	584		584	14
514	234	204	213	217		217	13
532	166	132	244	150		173	50
633	6	5	3	4		4	1

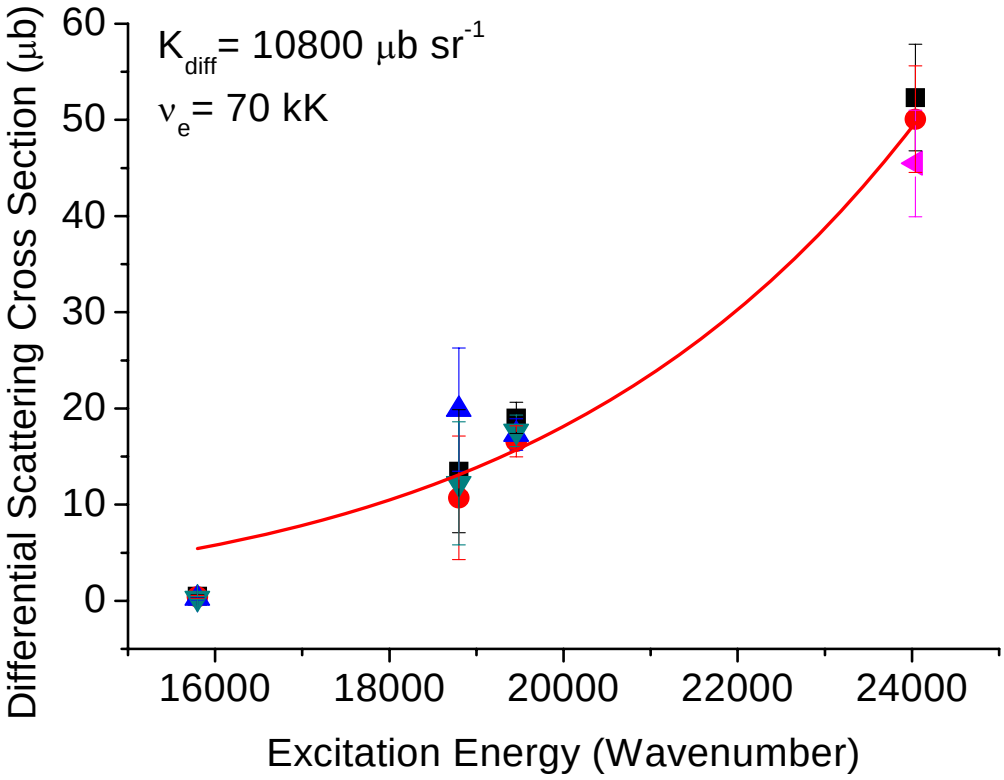

Figure 5.7: Plot of differential scattering cross section vs. excitation energy for the 1298 cm^{-1} band of $[Bu_4P]^+[(octyl)_2PO_2]^-$.

Table 5.16: The differential scattering cross sections of the 1447 cm^{-1} band of $[Bu_4P]^+[(octyl)_2PO_2]^-$.

Excitation Wavelength (nm)	Relative to Cyc μb sr^{-1}	Relative to Ctet μb sr^{-1}	Relative to Benz μb sr^{-1}	Relative to Dcm μb sr^{-1}	Relative to Aceto μb sr^{-1}	Average μb sr^{-1}	Std Dev μb sr^{-1}
416	119.42	115.48			110.94	115.28	4.25
487	79.47	70.37	68.45	70.54		72.21	4.93
514	59.50	51.93	54.14	55.25		55.20	3.18
532	33.08	26.30	48.28	29.96		34.40	9.65
633	0.78	0.63	0.76	0.93		0.77	0.13

Table 5.17: The absolute scattering cross sections of the 1447 cm^{-1} band of $[Bu_4P]^+[(octyl)_2PO_2]^-$.

Excitation Wavelength (nm)	Relative to Cyc μb	Relative to Ctet μb	Relative to Benz μb	Relative to Dcm μb	Relative to Aceto μb	Average μb	Std Dev μb
416	1415	1368			1314	1366	50
487	942	834	811	836		856	58
514	705	615	641	655		654	38
532	392	312	572	355		408	114
633	9	7	9	11		9	1

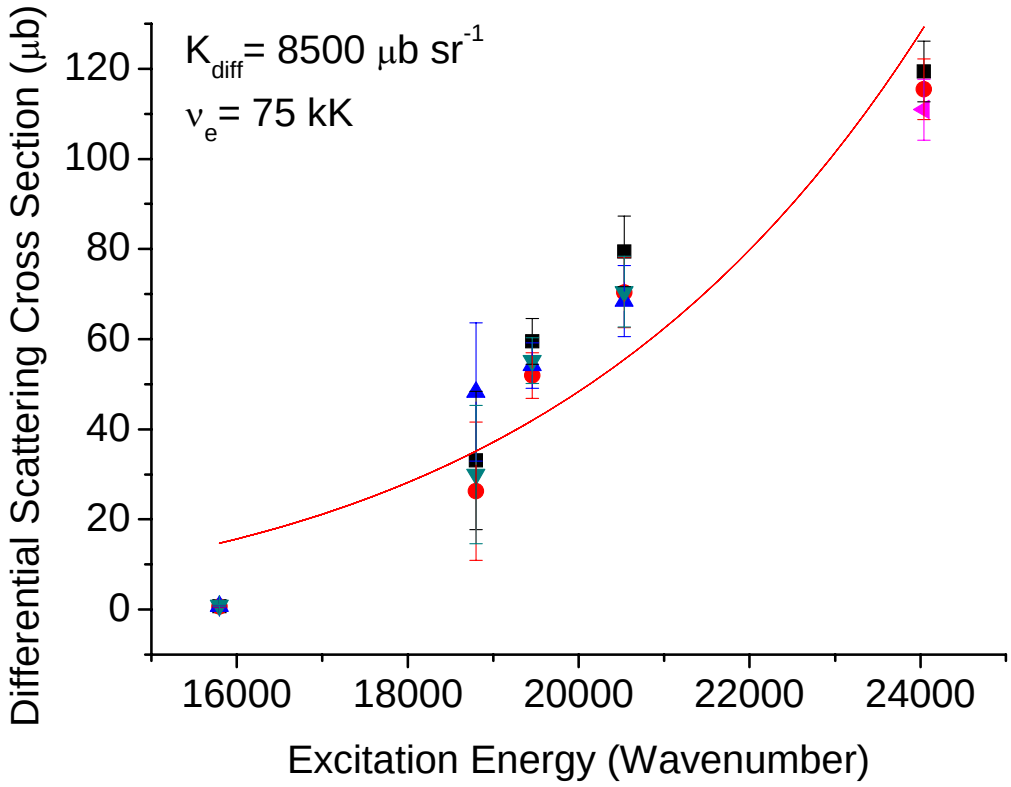

Figure 5.7: Plot of differential scattering cross section vs. excitation energy for the 1447 cm^{-1} band of $[Bu_4P]^+[(octyl)_2PO_2]^-$.

Table 5.18: Virtual excited state and differential coupling constant for the standards from literature [20-22].

Chemical Species	Raman Shift cm^{-1}	ν_e kK	K_{diff} $\mu b\ sr^{-1}$
Cyclohexane	802	115	90000
Carbon Tetrachloride	775	51	2243
Benzene	992	80	68000
Dichloromethane	704		

Note: 1 barn (b) = 10^{-24} cm^2, 1 $Å^2$ = 10^{-16} cm^2, 1 μb = 10^{-14} $Å^2$, 1 kK= 1000 cm^{-1}

Table 5.19: Virtual excited state and differential coupling constant for the ionic liquids obtained from A-term fitting.

Chemical Species	Raman Shift cm^{-1}	ν_e kK	K_{diff} $\mu b\ sr^{-1}$
$[CH_3N(C_4H_8)Bu]^+[(F_3CSO_2)_2N]^-$	741	135	33000
$[Et_3NH]^+[(octyl)PO_2H]^-$	1240	63	520
	1300	75	210
$[Bu_4N]^+[(hexyl)PO_2H]^-$	1452	75	2900
	1477	86	10300
$[Bu_4P]^+[(octyl)_2PO_2]^-$	1298	70	10800
	1447	75	8500

Note: 1 barn (b) = 10^{-24} cm^2, 1 $Å^2$ = 10^{-16} cm^2, 1 μb = 10^{-14} $Å^2$, 1 kK= 1000 cm^{-1}

Table 5.20: Virtual excited state and absolute coupling constant for the standards from literature [20-22].

Chemical Species	Raman Shift (cm^{-1})	ν_e (kK)	K μb
Cyclohexane	802	115	580000
Carbon Tetrachloride	775	51	768000
Benzene	992	80	26800

Note: 1 barn (b) = 10^{-24} cm^2, 1 $Å^2$ = 10^{-16} cm^2, 1 μb = 10^{-14} $Å^2$, 1 kK= 1000 cm^{-1}

Table 5.21: Virtual excited state and absolute coupling constant for the ionic liquids obtained from A-term fitting.

Chemical Species	Raman Shift (cm^{-1})	ν_e (kK)	K μb
$[CH_3N(C_4H_8)Bu]^+[(F_3CSO_2)_2N]^-$	741	135	320000
$[Et_3NH]^+[(octyl)PO_2H]^-$	1240	63	5700
	1300	75	2400
$[Bu_4N]^+[(hexyl)PO_2H]^-$	1452	75	35800
	1477	86	117000
$[Bu_4P]^+[(octyl)_2PO_2]^-$	1298	70	132800
	1447	75	100000

Note: 1 barn (b) = 10^{-24} cm^2, 1 $Å^2$ = 10^{-16} cm^2, 1 μb = 10^{-14} $Å^2$, 1 kK= 1000 cm^{-1}

5.4 Discussion of A-Term Fitting to Raman Data

Differential coupling constants of the solvents ranged from 2,000-100,000 μb sr^{-1} and effective excited state energy ranged from 50-120 kK. Similarly, differential coupling constants of the ionic liquids ranged from 210-33,000 μb sr^{-1} and effective excited state energy ranged from 53-135 kK. The absolute coupling constant of the standards ranged from 26,800-768,000 μb and the ionic liquids ranged from 2,400-320,000 μb. The differential scattering cross sections of the ionic liquids were also of the same order as the standards. To get a large scattering cross section a large value of K and a small value of ν_e is needed. Alternatively, a huge value of K and a large value of ν_e will also yield a large scattering cross section. Although the relative intensities of the ionic liquid bands are less than that of the standards they are broader due to the numerous modes present under a peak (see section 3.5), giving a larger scattering cross section.

Values for ν_e of 50kK correspond to a wavelength of 200 nm, which has enough energy to generate $\pi \rightarrow \pi^*$ and $n \rightarrow \pi^*$ transitions. Values for ν_e of 100kK correspond to a wavelength of 100 nm, which has enough energy to generate $\sigma \rightarrow \sigma^*$ transitions.

There are many possibilities for errors to be introduced in the determination of differential scattering cross sections and the parameters K and ν_e:

1. Experimental errors such as stray light, fluctuations in laser intensity and cell position will affect the raw data.
2. The wavelength range chosen for the peak area fitting will vary from each fitting.

3. Numerous steps are involved with spreadsheets that would compound errors as the data processing progressed.
4. The non-linear peak fitting module can find other unphysical parameters of K_{diff} and ν_e to also give a good fit to the data, as illustrated below.

This fit of the 742 cm^{-1} band of $[CH_3N(C_4H_8)Bu]^+[(F_3CSO_2)_2N]^-$ was obtained by the non-linear curve fitting program (Figure 5.8). The value of an effective excited state of 290 kK is unphysical; this would give a wavelength of 34 nm which corresponds to energy in the far UV / soft X-ray region, which is starting to strip electrons from the core levels of the molecule.

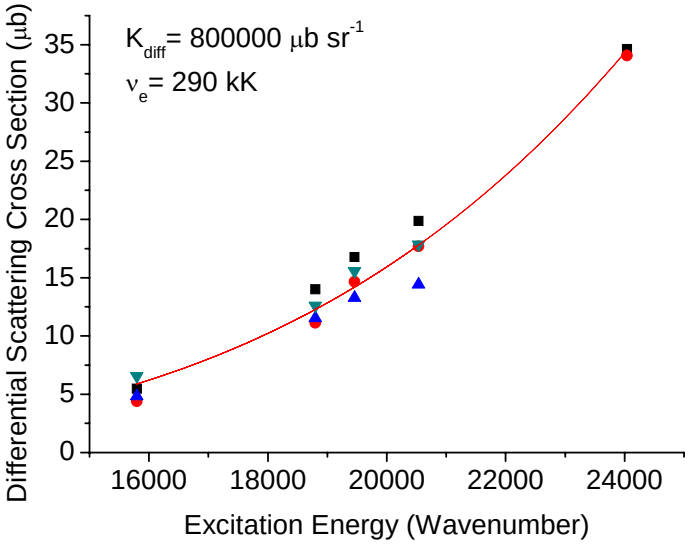

Figure 5.8: An unphysical A-term fit for the 742 cm^{-1} band of the ionic liquid $[CH_3N(C_4H_8)Bu]^+[(F_3CSO_2)_2N]^-$.

The 487 nm and 633 nm data have scattering cross sections that seem to be consistently lower than calculated. This could be due to the laser power of these wavelengths being too low to generate significant Raman scattering. A higher power laser or a more effective/longer collection would give stronger Raman bands allowing more accurate scattering cross sections.

Now that the ν_e value has been determined the use of a single A-term approximation may be justified. For sufficiently large ν_e the differences in excited state vibrational energies seem small and may be replaced by a single excited state, as illustrated in Figure 5.6. All of the experimental values of ν_e were 50 kK or greater, justifying the use of the single A-term approximation [4].

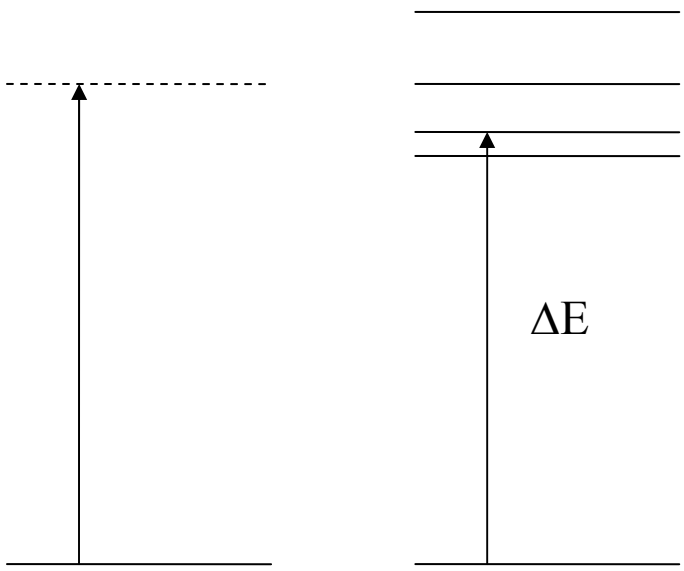

Figure 5.9: The replacement of multiple excited vibrational states with a single vibrational state for large ΔE.

Chapter 6

Conclusion

6.0 Conclusion

The differential and absolute scattering cross sections of vibrational modes of the ionic liquids $[CH_3N(C_4H_8)Bu]^+[(F_3CSO_2)_2N]^-$, $[Et_3NH]^+[(octyl)PO_2H]^-$, $[Bu_4N]^+[(hexyl)PO_2H]^-$ and $[Bu_4P]^+[(octyl)_2PO_2]^-$ were experimentally determined at wavelengths 416 nm, 487 nm, 514 nm, 532 nm and 633 nm. A-term plots were constructed with these results to obtain the parameters K_{diff}, K and ν_e. This allowed the calculation of the differential and absolute scattering cross sections at any wavelength.

The Raman spectra were found to be similar to the spectra predicted by Gaussian 03, implying that no underlying anomalous effects were perturbing the vibrational modes. The experimental Raman and infrared peaks were found to be broad and intertwined, the use of Gaussian calculations showed that this was due to the close proximity of numerous vibrational bands.

At the conclusion of this project the Raman equipment and procedures have been set up for operation at Massey University for future students who follow.

6.1 Future Work

The first step in understanding the electron transfer rate of ionic liquids has been completed. In this thesis the coupling constant K and effective excited state energy ν_e has been obtained, hence the absolute scattering cross section can be calculated for any wavelength. The next step is to put a probe dye molecule like disperse red in to the ionic liquid and take the Raman spectrum. This time the scattering cross section of the dye's modes will be determined using the known ionic liquid bands as standards. By looking at the dyes properties the reorganisation energy of the ionic liquid can be determined. Finally with the reorganisation energy known a Marcus Hush model can be used to investigate the electron transfer rate. This is important when considering ionic liquids as materials in new devices.

The Rayleigh bands of the ionic liquids can also be investigated in addition to the Raman bands, to determine the magnitude of the polarizability. The polarizability can indicate the size of the columbic forces and if they are the dominant interaction responsible for the ionic liquid being in the liquid phase.

The ionic liquids analogous isoelectronic neutral binary solution could be investigated by Raman spectroscopy to observe if any major differences occur [23]. This would involve the cation's nitrogen being replaced with a carbon atom and the anion's phosphorus with a silicon atom.

These projects can be easily investigated incrementally with honours or masters projects, without exceeding the expertise of the institute or the equipment available.

References

1. Skoog, D.A., *Principles of instrumental analysis.* 5th ed. Harcourt Brace College Publishers.
2. Long, D.A., *Raman spectroscopy.* 1977. New York: McGraw-Hill.
3. Erzinger, D.J., *Inorganic and Isotope Geochemistry*. April 2000.
4. Clark, R.J.H. and Dines, T.J., *Resonance Raman spectroscopy and its application to inorganic chemistry.* Angewandte Chemie, 1986. **98**(2): p. 131-60.
5. Jarzecki, A.A. and T.G. Spiro, *Porphyrin Distortion from Resonance Raman Intensities of Out-of-Plane Modes: Computation and Modeling of N-Methylmesoporphyrin, a Ferrochelatase Transition State Analog.* Journal of Physical Chemistry A, 2005. **109**(3): p. 421-430.
6. Trulson, M.O. and Mathies, R.A., *Raman cross section measurements in the visible and ultraviolet using an integrating cavity: application to benzene, cyclohexane, and cacodylate.* Journal of Chemical Physics, 1986. **84**(4): p. 2068-74.
7. Earle, M.J., et al., *The distillation and volatility of ionic liquids.* Nature, 2006. **439**(7078): p. 831-834.
8. Katsyuba, S.A., et al., *Molecular structure, vibrational spectra, and hydrogen bonding of the ionic liquid 1-ethyl-3methyl-1H-imidazolium tetrafluoroborate.* Helvetica Chimica Acta, 2004. **87**(10): p. 2556-2565.
9. Forsyth, S.A., Pringle, J.M., MacFarlane, D.R. *Ionic Liquids-An Overview.* Australian Journal of Chemistry, 2004. **57**(2): p. 113-119.
10. Mazille, F., et al., *Influence of Ionic Liquids Bearing Functional Groups in Dye-Sensitized Solar Cells.* Inorganic chemistry, 2006. **45**: p. 1585-1590.
11. Parker, S.T., et al., *Improved Turn-on Times of Iridium Electroluminescent Devices by Use of Ionic Liquids.* Chemistry of Materials, 2005. **17**(12): p. 3187-3190.
12. Welton, T., *Room-Temperature Ionic Liquids. Solvents for Synthesis and Catalysis.* Chemical Reviews (Washington, D. C.), 1999. **99**(8): p. 2071-2083.
13. McCreery, R.L. *http://www.chemistry.ohio-state.edu/~rmccreer/freqcorr/images/toluene.html*. 2006.

14. Glover, W.J. and Madden, P.A., *Raman spectra of ionic liquids: A simulation study of LaCl3 and its mixtures with alkali chlorides.* Journal of Chemical Physics, 2004. **121**(15): p. 7293-7303.
15. Foresman, J.B. and Frisch, A., *Exploring Chemistry with Electronic Structure Methods*. 2nd ed. 1996: USA.
16. Waterland, M.R., et al., *Structural Changes upon Photoexcitation into the Metal-to-Ligand Charge-Transfer State of [Cu(pqx)(PPh$_3$)$_2$]+ Probed by Resonance Raman Spectroscopy and Density Functional Theory.* Journal of Physical Chemistry A, 2005. **109**: p. 8826-8833.
17. Evans, E.W., George, W.O., Platts, J.A., *Ab initio and DFT computer studies of complexes of trimethylphosphine and products of substituted phosphonium cations with hydroxide, chloride and fluoride anions: Phosphorus analogues of choline and acetylcholine.* Theochem, 2005. **730**(1-3): p. 185-197.
18. Silverstein, R.M. and Webster, F.X., *Spectrometric identification of organic compounds*. 1998: John Wiley & Sons, Inc.
19. Kemp, W., *Organic Spectrscopy*. 3rd ed. 1991: MacMillian press ltd.
20. Zong, R.F. and Thummel, R.P., *2,9-di-(2 '-pyridyl)-1,10-phenanthroline: A tetradentate ligand for Ru(II).* Journal of the American Chemical Society, 2004. **126**(35): p. 10800-10801.
21. McCreery, R.L., *Raman Spectroscopy for Chemical Analysis*. A Series of Monographs on Analytical Chemistry and its Applications. 2000: John Wiley & Sons, Inc. United States of America.
22. Chambers, J.M. and Griffiths, P.R., *Handbook of Vibrational Spectroscopy*. 2002: John Wiley & Sons Ltd, Chichester.
23. Shirota, H. and Castner, E.W., *Physical Properties and Intermolecular Dynamics of an Ionic Liquid Compared with Its Isoelectronic Neutral Binary Solution.* Journal of Physical Chemistry A, 2005. **109**(42): p. 9388-9392.